

The mechanics of tidal streams

Andy Eyre* and James Binney

Rudolf Peierls Centre for Theoretical Physics, 1 Keble Road, Oxford OX1 3NP, UK

5 June 2022

ABSTRACT

We present an analysis of the mechanics of thin streams, which are formed following the tidal disruption of cold, low-mass clusters in the potential of a massive host galaxy. The analysis makes extensive use of action-angle variables, in which the physics of stream formation and evolution is expressed in a particularly simple form. We demonstrate the formation of streams by considering examples in both spherical and flattened potentials, and we find that the action-space structures formed in each take on a consistent and characteristic shape. We demonstrate that tidal streams formed in realistic galaxy potentials are poorly represented by single orbits, contrary to what is often assumed. We further demonstrate that attempting to constrain the parameters of the Galactic potential by fitting orbits to such streams can lead to significant systematic error. However, we show that it is possible to predict accurately the track of streams from simple models of the action-space distribution of the disrupted cluster.

Key words: methods: analytical – methods: numerical – Galaxy: kinematics and dynamics – Galaxy: halo – Galaxy: structure – galaxies: interactions

1 INTRODUCTION

Recent years have seen a tremendous advance in the quality and quantity of observational data for substructure in the halo of our Galaxy. Of particular note is the outstanding success of the Sloan Digital Sky Survey (SDSS, York et al. 2000), which has uncovered large numbers of streams in the halo of the Milky Way (Odenkirchen et al. 2003; Majewski et al. 2003; Yanny et al. 2003; Belokurov et al. 2006, 2007; Grillmair 2006; Grillmair & Dionatos 2006; Grillmair & Johnson 2006; Grillmair 2009; Newberg et al. 2009). These streams appear to be the relics of tidally stripped globular clusters and dwarf galaxies that have fallen into the Galaxy, although it is often the case that no obvious progenitor object can be associated with a particular stream.

It has been empirically noted that such tidal streams appear to delineate the orbit of the progenitor object from which they formed (McGlynn 1990; Johnston et al. 1996). A consequence of this assumption is that measurements of separate segments of a single stream can be equated to sampling different phases of a single orbit. If either complete phase-space information (Willett et al. 2009), or a certain subset of it (Jin & Lynden-Bell 2007; Binney 2008; Eyre & Binney 2009a), is known for a sequence of phases along a single orbit, it is possible to diagnose the Galactic potential with exquisite precision (Binney 2008). Thus the assumption that such streams delineate orbits promises tremendous diagnostic power and had been frequently invoked (Binney 2008; Eyre & Binney 2009a; Odenkirchen et al. 2009; Willett et al. 2009; Koposov et al. 2010; Eyre 2010a).

Such techniques are hampered by the considerable difficulty in obtaining observational data of adequate precision for stars in distant streams. More worrisome, however, is the mounting evidence that streams do not precisely delineate orbits (Dehnen et al. 2004; Choi et al. 2007; Montuori et al. 2007; Eyre & Binney 2009b)—in these circumstances, which we will demonstrate to be generic—any conclusions drawn from the fitting of orbits to streams could be systematically in error.

It is therefore of vital importance for the continued application of such techniques that we obtain an understanding of the relationship between tidal streams and the orbits of the stars that comprise them. In particular, we must determine under what circumstances tidal streams delineate orbits, by what measure they are in error when they do not, and what can be done to correct this error. There has not to date been an exposition of stream formation that fundamentally addresses these issues.

Most studies have either focused on N-body simulations (Choi et al. 2007; Montuori et al. 2007), the confusion of which makes the predominant physics hard to isolate, or have attempted to describe the problem in terms of conventional phase-space coordinates and classical integrals (Dehnen et al. 2004; Choi et al. 2007), which makes the problem intractably hard. The work of Choi et al. (2007) made some progress towards understanding the dynamical structure of clusters at the point of disruption, and they provide a qualitative picture of the evolution of tidal tails, understood in terms of classical integrals. However, they are unable to make predictions for stream tracks on the basis of this picture alone, and they are ultimately forced to rely on N-body simulation for quantitative results. In this paper, we approach the problem using action-angle

* Email: eyre@thphys.ox.ac.uk

variables, in which the physics of stream formation finds a natural and simple expression (Helmi & White 1999; Tremaine 1999).

We confine our investigation to the formation of long, cold streams, such as may form from tidally disrupted globular clusters. We do so for two reasons. First, a low mass for the progenitor cluster simplifies the description of its orbital mechanics, because of the lack of dynamical friction and other feedback effects in its interaction with the host galaxy. Second, thin, long streams provide the strongest constraints upon the Galactic potential, because any orbit delineated by them can be observationally identified with less ambiguity (Binney 2008; Eyre & Binney 2009b). Hence, it is long, cold streams that are of primary interest for use as probes of the potential.

We study the mechanics of stream formation immediately following the tidal disruption of a progenitor cluster. In much of the work that follows, the assumption is made that stream stars feel only the potential of the Galaxy, i.e. the stream stars do not self-gravitate. This assumption is generally a fair one: the stars in streams are generally spaced too widely for their self-gravity to be of consequence (Dehnen et al. 2004). Indeed, we will demonstrate below that self-gravity becomes negligible shortly after stars are stripped from our model clusters.

The remainder of the paper is arranged as follows: Section 2 discusses the action-angle variables in which we perform our analysis. Section 3 discusses the basic mechanics of stream formation and propagation. Section 4 discusses the detail of stream formation in spherical systems, with the aid of some examples. Section 5 relates the action-angle structure of streams to the corresponding real-space manifestation. Section 6 examines the action-space distribution of disrupted clusters using N-body simulation. Section 7 describes the consequences of optimising potential parameters under the faulty assumption that streams follow orbits. Section 8 discusses stream formation in flattened systems, using an axisymmetric Stäckel potential as an example. Finally, Section 9 presents our concluding remarks.

2 ACTION-ANGLE VARIABLES

We use action-angle variables to analyse stream formation and propagation. The usefulness and theoretical basis of action-angle variables is extensively discussed in §3.5 of Binney & Tremaine (2008; hereafter BT08).

Action-angle variables are a set of canonical coordinates, like Cartesian phase-space coordinates, that can be used to describe systems in Hamiltonian mechanics. Actions \mathbf{J} are useful because they are constants of motion. Moreover, the angle variables $\boldsymbol{\theta}$ that are conjugate to them evolve linearly in time

$$\boldsymbol{\theta}(t) = \boldsymbol{\theta}(0) + \boldsymbol{\Omega}t, \quad (1)$$

where we have introduced the frequencies

$$\Omega_i(\mathbf{J}) \equiv \dot{\theta}_i = \frac{\partial H}{\partial J_i}. \quad (2)$$

Hence, the motion of a system described by action-angle variables is very easy to predict.

§3.5 of Binney & Tremaine 2008 discusses at length the calculation of action-angle coordinates in various systems. Here, we note that standard methods for calculating action-angle coordinates require the Hamilton-Jacobi equation to separate (§3.5.1 of BT08). This condition is met by all spherically symmetric potentials, but excludes any non-spherical potential that is not of Stäckel form (see

Section 8.1 below). Given separability, the action corresponding to a coordinate q is given by

$$J_q = \frac{1}{2\pi} \oint p_q dq, \quad (3)$$

where the integral is over the closed path that encloses a single oscillation of the coordinate q along an orbit.

We note that just as spherical systems are naturally described by spherical polar coordinates (r, ϑ, ϕ) , the natural actions for such systems are (J_r, L) , where J_r is the radial action, and $L = J_\vartheta + |L_z|$ is the angular momentum. Throughout this paper, and without loss of generality, when spherical systems are under study we set $L = L_z$ and confine the motion to the (x, y) plane.

In the sections that follow, we utilize the equations from §3.5.2 of BT08 to transform between the action-angle coordinates $(J_r, L, \theta_r, \theta_\phi)$ and conventional phase-space coordinates, when investigating spherical potentials. The action-angle coordinates used when investigating non-spherical potentials are discussed in Section 8.1 below.

3 THE FORMATION OF STREAMS IN ACTION-ANGLE SPACE

Consider a low-mass cluster that has recently been tidally disrupted, with just enough time having passed so that the stripped stars no longer feel the effects of one another's gravity. The cluster is on a regular orbit, identified by its actions \mathbf{J}_0 , in a fixed background potential, which has a Hamiltonian $H(\mathbf{J})$. Suppose further that in the locality of \mathbf{J}_0 , the Hamiltonian is well described by the Taylor expansion,

$$H(\mathbf{J}) = H_0 + \boldsymbol{\Omega}_0 \cdot \delta\mathbf{J} + \frac{1}{2} \delta\mathbf{J}^T \cdot \mathbf{D} \cdot \delta\mathbf{J}, \quad (4)$$

where $\delta\mathbf{J} = \mathbf{J} - \mathbf{J}_0$, \mathbf{D} is the Hessian of H

$$D_{ij} = \left. \frac{\partial^2 H}{\partial J_i \partial J_j} \right|_{\mathbf{J}_0}, \quad (5)$$

and $\boldsymbol{\Omega}_0$ is the frequency vector of the cluster's orbit

$$\Omega_{0,i} = \left. \frac{\partial H}{\partial J_i} \right|_{\mathbf{J}_0}. \quad (6)$$

The frequency vector $\boldsymbol{\Omega}$ of a nearby orbit \mathbf{J} is then

$$\boldsymbol{\Omega}(\mathbf{J}) = \boldsymbol{\Omega}_0 + \mathbf{D} \cdot \delta\mathbf{J}. \quad (7)$$

If the disrupted cluster has some spread in actions $\Delta\mathbf{J}$ and angles $\Delta\boldsymbol{\theta}_0$, corresponding to the spread in position and velocity of its constituent stars, then the spread in angle-space after some time t is given by (Helmi & White 1999; Tremaine 1999; BT08 §8.3.1),

$$\Delta\boldsymbol{\theta}(t) = t\Delta\boldsymbol{\Omega} + \Delta\boldsymbol{\theta}_0 \simeq t\Delta\boldsymbol{\Omega}, \quad (8)$$

where the near equality is valid when $t\Delta\boldsymbol{\Omega} \gg \Delta\boldsymbol{\theta}_0$, and where we have introduced the spread in frequencies, $\Delta\boldsymbol{\Omega}$, which are related to the spread in actions via

$$\Delta\boldsymbol{\Omega} = \mathbf{D} \cdot \Delta\mathbf{J}. \quad (9)$$

In the absence of self-gravity, the action-space distribution $\Delta\mathbf{J}$ is frozen for all time. \mathbf{D} and $\boldsymbol{\Omega}$ are functions of \mathbf{J} only, and so are similarly frozen. The secular evolution of a disrupted cluster is therefore to spread out in angle-space, with its eventual shape determined by $\Delta\boldsymbol{\Omega} = \mathbf{D} \cdot \Delta\mathbf{J}$, and its size growing linearly with t .

For a given $\Delta\mathbf{J}$, what does $\Delta\boldsymbol{\Omega}$ look like? Equation (8) and

equation (9) show that \mathbf{D} acts as a linear map between a star's position in action-space and its position in angle-space. \mathbf{D} is a symmetric matrix, so it is characterised by its mutually orthogonal eigenvectors $\hat{\mathbf{e}}_n$ ($n = 1, 3$) and its real eigenvalues λ_n .

Consider a cluster whose stars are distributed isotropically within a unit sphere in action-space centred on \mathbf{J}_0 . The corresponding angle-space structure, resulting from the mapping of this sphere by \mathbf{D} , will be an ellipsoid with semi-axes of length $t\lambda_n$ and direction $\hat{\mathbf{e}}_n$.

If the λ_n are finite and approximately equal, such an isotropic cluster will spread out in angle-space with no preferred direction. Eventually, the cluster will uniformly populate the whole of angle-space. In real-space the cluster will uniformly fill the entire volume occupied by the orbit \mathbf{J}_0 : such a cluster would not form a stream.

If one of the λ_n is much smaller than the others, then \mathbf{D} will map the cluster into a highly flattened ellipsoid in angle-space. In real-space, the cluster will occupy a 2-dimensional subspace of the orbital volume of \mathbf{J}_0 . The precise configuration of this subspace is likely to be complex, but it would not form a stream.

If two of the λ_n are small, then \mathbf{D} maps the cluster into a line in angle-space. In this case, the resulting real-space structure will be a filament. The density of this filament will fall linearly with t . In a real galaxy, such a structure may therefore persist with a significant overdensity for some time. It is this case that describes the formation of tidal streams (§8.3.1 of BT08) investigated in detail in this paper. Finally, if all the λ_n are zero, there will be no spread, and even an unbound cluster will remain extant indefinitely.

We note that there is no *a priori* reason for any of the λ_n to be small. The existence of \mathbf{D} imposes no conditions on H in general, save that it must be twice differentiable near to \mathbf{J}_0 . We can write a Hamiltonian for which, for a particular \mathbf{J}_0 at least, the λ_n and the $\hat{\mathbf{e}}_n$ take any specified values. It must therefore be a peculiar property of realistic galactic potentials that causes disrupted clusters to form streams.

3.1 Validity

Let us consider briefly the validity of the preceding analysis. The key assumption is that the Taylor expansion (4) holds, which it does if

$$\delta J_{ij} \gg \frac{1}{3} \frac{\partial D_{ij}}{\partial J_k} \delta J_k = \frac{1}{3} \frac{\partial^3 H}{\partial J_i \partial J_j \partial J_k} \delta J_k. \quad (10)$$

If H is dominated by some low power of J , this condition becomes

$$\delta J_i \ll J_i. \quad (11)$$

In general then, we expect our analysis to be valid if the spread in action of the stars in the cluster is small compared to the actions themselves, which is likely to be true for cold clusters on high-energy orbits around massive hosts. The condition (10) is met in detail for all the examples considered in this paper.

3.2 The problem

We have seen that the condition for a stream to form is that one of the eigenvalues λ_n of the linear map, \mathbf{D} , must be much larger than the other two. Herein, we will number the λ_n and their corresponding $\hat{\mathbf{e}}_n$ such that

$$\lambda_1 > \lambda_2 \geq \lambda_3. \quad (12)$$

Under what conditions does the direction of this stream point along the progenitor's orbit?

Taken over a short period of time—say, the time taken for an individual star to travel along the length of a stream—every star in the stream will follow an almost identical trajectory. If phase is disregarded and the trajectories superimposed, they would overlay almost perfectly. Streams form because *slight* differences between the trajectories of individual stars grow secularly over the lifetime of a stream, which may be many orbital periods of the individual stars. There is no fundamental dynamical reason why the track of the resulting stream should delineate the progenitor's orbit, nor the orbit of any one of the stars, nor any orbit in the governing potential.

In action-angle coordinates, the trajectory in angle-space of an orbit \mathbf{J} is given by the frequency vector, $\boldsymbol{\Omega}(\mathbf{J})$. A necessary condition for a stream to delineate precisely the progenitor orbit is that the long axis of the angle-space distribution $\Delta\boldsymbol{\theta}$ is aligned with the progenitor frequency $\boldsymbol{\Omega}_0$. However, we shall see in Section 5.3 that because real-space position $\mathbf{x}(\mathbf{J}, \boldsymbol{\theta})$ is a function of \mathbf{J} as well as angle $\boldsymbol{\theta}$, this condition alone is *not* sufficient to ensure real-space alignment between streams and orbits.

We note that the angle-space distribution, $\Delta\boldsymbol{\theta}$, depends on both the potential, \mathbf{D} , and the action-space distribution, via $\Delta\mathbf{J}$, and in practical cases it is necessary to consider both when determining its gross alignment.

The problem of stream formation and evolution is patently a complicated one. To further our analysis, we will examine separately the role of the linear map \mathbf{D} , the real-space map $\mathbf{x}(\mathbf{J}, \boldsymbol{\theta})$, and the action-space distribution $\Delta\mathbf{J}$. Having done so, we will proceed to use this understanding to examine the formation of streams in practical cases.

4 THE LINEAR MAP \mathbf{D} IN SPHERICAL CASES

In order to analyze the behaviour of the linear map, let us restrict ourselves to a case in which our cluster is both isotropic and small in $\Delta\mathbf{J}$. The angle-space distribution $\Delta\boldsymbol{\theta}$ is now an ellipsoid with semi-axes of length λ_n , and with the semi-major axis of the distribution aligned with the principal direction of the linear map, $\hat{\mathbf{e}}_1$. In this scenario, the stream will be delineated by a single orbit if the condition

$$\hat{\mathbf{e}}_1 = \hat{\boldsymbol{\Omega}}_0, \quad (13)$$

is met, since $\Delta\mathbf{J}$ is small and so $\mathbf{x}(\mathbf{J}, \boldsymbol{\theta}) \simeq \mathbf{x}(\mathbf{J}_0, \boldsymbol{\theta})$.

We will proceed by examining the forms of $\boldsymbol{\Omega}$ and \mathbf{D} , and hence the angle-space geometry of streams, for some example spherical potentials. We remind ourselves that such systems can always be completely described by two actions.

4.1 Kepler potential

There are remarkably few potentials of interest for which the Hamiltonian can be written as a function of \mathbf{J} in closed form. One such potential is the Kepler potential

$$\Phi(r) = -\frac{GM}{r}, \quad (14)$$

for which the Hamiltonian is,

$$H(\mathbf{J}) = -\frac{(GM)^2}{2(J_r + L)}, \quad (15)$$

where J_r is the radial action, and L is the angular momentum. The frequencies can be worked out by direct differentiation, giving

$$\boldsymbol{\Omega} = \begin{pmatrix} \Omega_r \\ \Omega_\phi \end{pmatrix} = \frac{(GM)^2}{2(J_r + L)} \begin{pmatrix} 1 \\ 1 \end{pmatrix}. \quad (16)$$

Table 1. Actions and apses for selected orbits in the spherical potentials used in this paper. We generally choose $J_\phi = L$ so all orbits remain in the (x, y) plane.

	$J_r / \text{kpc km s}^{-1}$	$L / \text{kpc km s}^{-1}$	r_p / kpc	r_a / kpc
K1	780.	1016.	1.5	13
I1	313.	1693.	5	13
I2	0.	1920.	8	8
I3	207.	1920.	6	12.5
I4	215.4	3127.	11	20
I5	571.7	2536.	7	20

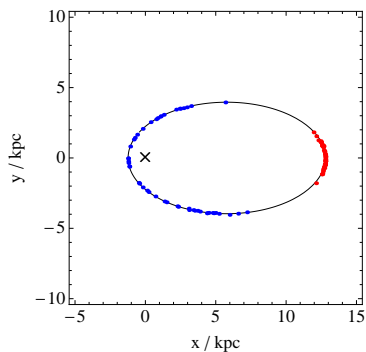


Figure 1. The solid line shows the orbit K1 (Table 1) in a Kepler potential, on which a cluster of 50 test particles has been evolved. The particles were released at apocentre. The red dots show the positions of the test particles near apocentre, after 24 complete orbits, at $t = 4.02$ Gyr. The blue dots show the same test particles near pericentre, approximately half an orbit later. In both cases, the dots delineate the progenitor orbit precisely.

The linear map \mathbf{D} is calculated via a further round of differentiation, and has eigenvalue/vector pairs

$$[\lambda_1, \hat{\mathbf{e}}_1] = \left[\lambda_1, \begin{pmatrix} e_{1,r} \\ e_{1,\phi} \end{pmatrix} \right] = \left[\frac{-2(GM)^2}{(J_r + L)^3}, \begin{pmatrix} 1 \\ 1 \end{pmatrix} \right], \quad (17)$$

$$[\lambda_2, \hat{\mathbf{e}}_2] = \left[\lambda_2, \begin{pmatrix} e_{2,r} \\ e_{2,\phi} \end{pmatrix} \right] = \left[0, \begin{pmatrix} -1 \\ 1 \end{pmatrix} \right]. \quad (18)$$

The linear map \mathbf{D} has only one finite eigenvalue, and so the Kepler potential will always form streams from disrupted clusters. Further, we observe that since $\hat{\mathbf{e}}_1 \propto \boldsymbol{\Omega}$ in all circumstances, streams will always perfectly delineate progenitor orbits in Kepler potentials, regardless of the action-space distribution of the cluster from which they form. In this potential streams exhibit secular spread strictly along the orbit, and do not grow wider with time.

4.1.1 Numerical tests

We have confirmed the above prediction numerically. We use a Kepler potential with mass $M = 1.75 \times 10^{11} M_\odot$, which reproduces a fiducial circular velocity $v_c = 240 \text{ km s}^{-1}$ at the approximate solar radius of $R_0 = 8 \text{ kpc}$. A cluster of 50 test particles was created, sampled from a Gaussian distribution in action-angle space, defined by $\sigma_J = 1 \text{ kpc km s}^{-1}$ and $\sigma_\theta = 5 \times 10^{-3}$ radians. This cluster was placed on the orbit K1, given in Table 1, in the aforementioned Kepler potential. The orbit is highly eccentric, with a pericentre radius of about 1.5 kpc and an apocentre of about 13 kpc.

The cluster was released at apocentre, and evolved for 4.02 Gyr, equal to 24 complete orbits, by integrating the equations

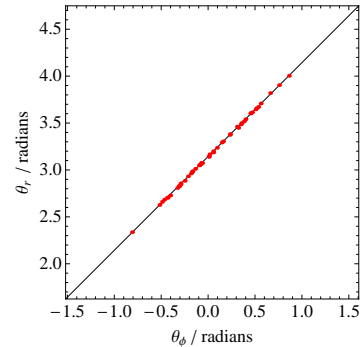


Figure 2. Angle-space configuration for the particles shown at apocentre in Fig. 1. The solid line shows the frequency vector $\boldsymbol{\Omega}_0$, with which the stream particles are perfectly aligned. Notably, there is no secular spread in the direction perpendicular to the stream motion, as predicted in Section 4.1.

of motion for each particle. Fig. 1 shows the real-space configuration of the particles at the end of this time, and Fig. 2 shows the configuration of the same particles in angle-space.

The cluster has elongated to form a stream that Fig. 1 shows to cover approximately half the orbit when the centroid is at pericentre. The stream does not spread in width in either real-space or angle-space. In both figures, the stream delineates the cluster's orbit perfectly. Fig. 1 shows that this is true irrespective of the real-space location of the centroid, so the prediction of the preceding section is validated.

4.2 Spherical harmonic oscillator

The spherical harmonic oscillator potential

$$\Phi(r) = \frac{1}{2} \Omega^2 r^2, \quad (19)$$

where Ω is a constant, applies for motion within a sphere of uniform density (§3.1a of BT08), and is therefore of relevance to galaxy cores in the absence of a black hole. The Hamiltonian is

$$H(J_r, L) = \Omega(L + 2J_r), \quad (20)$$

and the frequencies are

$$\boldsymbol{\Omega} = \begin{pmatrix} \Omega_r \\ \Omega_\phi \end{pmatrix} = \Omega \begin{pmatrix} 2 \\ 1 \end{pmatrix}, \quad (21)$$

while \mathbf{D} is a null matrix, implying that the eigenvalues are identically zero.

From this latter fact, we conclude that clusters in harmonic potentials will always remain in the same configuration in angle-space, and will not spread out. Hence, streams cannot form in harmonic potentials. We further note that, in any case, it would be difficult to tidally strip a cluster in a harmonic potential, since the tidal force dF_{tide} across a cluster

$$dF_{\text{tide}} \simeq \frac{\partial^2 \Phi}{\partial r^2} dr = \Omega^2 dr, \quad (22)$$

is independent of galactocentric radius r . Thus, a cluster that is bound at apocentre in such a potential will remain bound elsewhere along its orbit.

4.3 Isochrone potential

The isochrone potential (§2.2.2d of BT08) is a simple potential which has several useful properties. It behaves as a harmonic oscil-

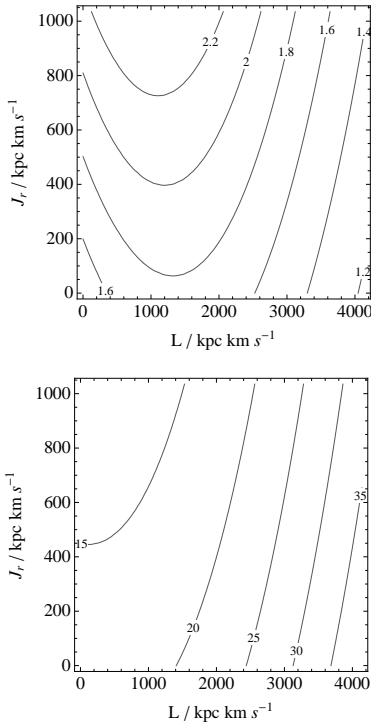


Figure 3. Details of the stream geometry in the isochrone potential of Section 4.3. Upper panel: the misalignment angle ϑ , in degrees, between the principal direction of \mathbf{D} and $\hat{\Omega}_0$, shown as a contour plot against the actions of the progenitor orbit. In all cases, ϑ is between 1.2 deg and 2.2 deg in angle-space. Lower panel: The ratio of the eigenvalues λ_1/λ_2 . The ratio is > 10 everywhere and rises sharply with increasing L . The actions shown in both plots cover a range of interesting orbits, which are described in Table 2.

lator in the limit of small radius, and as a Kepler potential at large radius, thus providing a reasonable model for a spherical galaxy across all radii. The form of the potential is

$$\Phi(r) = -\frac{GM}{b + \sqrt{b^2 + r^2}}, \quad (23)$$

where b is a constant scale. The Hamiltonian is

$$H(\mathbf{J}) = -\frac{(GM)^2}{2[J_r + \frac{1}{2}(L + \sqrt{L^2 + 4GMb})]^2}. \quad (24)$$

To proceed, we require the frequencies, which are obtained by partial differentiation of equation (24)

$$\Omega_r = \frac{(GM)^2}{[J_r + \frac{1}{2}(L + \sqrt{L^2 + 4GMb})]^3}, \quad (25)$$

$$\Omega_\phi = \frac{1}{2} \left(1 + \frac{L}{\sqrt{L^2 + 4GMb}} \right) \Omega_r. \quad (26)$$

To construct \mathbf{D} , we also require the derivatives of the frequencies with respect to the actions, which are obtained directly from equations (25) and (26).

The algebraic forms of both Ω and \mathbf{D} are untidy, and little progress can be made by simply inspecting them. Instead, we proceed by working numerically with a specific example. We use the isochrone potential with the parameters $M = 2.852 \times 10^{11} M_\odot$, $b = 3.64$ kpc, which is chosen to have a rotation curve maximized with $v_c = 240$ km s $^{-1}$ at the fiducial solar radius of $R_0 = 8$ kpc.

What then is the geometry of streams formed in this potential?

Table 2. The coordinate extrema of selected orbits from Fig. 3, illustrating the variety of orbits covered by that figure. The actions are expressed in kpc km s $^{-1}$, while the apses are in kpc.

J_r	L	r_p	r_a
1000	4000	13	46
1000	~ 0	~ 0	12
0	4000	20.3	20.3

Fig. 3 shows the misalignment angle between $\hat{\Omega}_0$ and $\hat{\mathbf{e}}_1$, given by

$$\vartheta = \arccos(\hat{\Omega}_0 \cdot \hat{\mathbf{e}}_1), \quad (27)$$

as well as the ratio of the eigenvalues λ_1/λ_2 , both as functions of \mathbf{J} . The range of \mathbf{J} shown in Fig. 3 covers a variety of interesting orbits, described in Table 2.

The upper panel shows that the principal direction of \mathbf{D} is misaligned with the progenitor orbit by 1–2 deg for all values of \mathbf{J} . The misalignment is at a minimum for both low energy and high energy circular orbits, and at a maximum for eccentric orbits with a guiding centre close to $r = b$. The lower panel shows that the ratio of the eigenvalues λ_1/λ_2 varies from 15 to 35 across the range, with the ratio maximized for high energy circular orbits, and minimized for high energy plunging orbits.

On this basis, we expect an isotropic cluster of test particles in this potential to form a stream in angle-space that is misaligned with $\hat{\Omega}_0$ by 1–2 deg and is 15–35 times longer than it is wide. Notably, such a stream is precluded from being delineated by any single orbit, close to \mathbf{J}_0 , in the correct isochrone potential.

4.3.1 Numerical tests

We created a cluster of 150 test particles, randomly sampled from a Gaussian distribution in action-angle space, defined by $\sigma_J = 0.2$ kpc km s $^{-1}$ and $\sigma_\theta = 10^{-3}$ radians. This cluster was placed on the orbit I1 from Table 1, which has an apocentre radius of ~ 13 kpc and a pericentre radius of ~ 5 kpc.

The cluster was released at apocentre, and evolved for 94 complete azimuthal circulations, equal to a period of $t = 22.75$ Gyr. Fig. 4 shows the angle-space configuration of the particles after this time. The arrowed, black line shows the orbit of the underlying cluster, $\hat{\Omega}_0$. The dashed line shows a straight line fit to the distribution of particles, which is clearly misaligned with the black line. We further note that, unlike the stream in the Kepler potential shown in Fig. 2, this stream has clearly increased in width since inception.

We can predict the shape of this distribution precisely. Plotted as a red ellipse in Fig. 4 is the angle-space image under \mathbf{D} of a circle in action-space. After some time, the angle-space distribution of an isotropic cluster of test particles should take the form of a scaled version of this image. We see that the image and the particle distribution are indeed comparable, and that the dashed line is perfectly aligned with the principal axis of the image.

How does this misalignment manifest itself in real-space? Fig. 5 shows the real-space configuration of the cluster at the end of the simulation. The orbit of the cluster is drawn with a solid black line, while the dashed line is a quadratic curve that has been least-squares fitted to the particle data.

The progenitor orbit is clearly a poor representation of the stream. Although the orbit passes through the centroid of the stream, as expected, the curvature of the orbit is too low to match

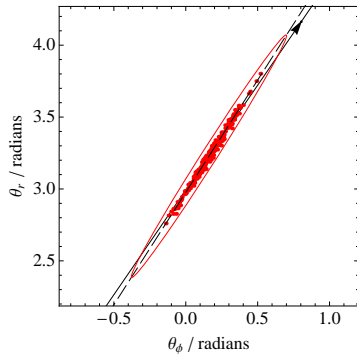


Figure 4. The angle-space distribution of a cluster of test particles, evolved on orbit II in the isochrone potential of Section 4.3.1 for 94 complete azimuthal circulations. The particles are shown at apocentre. The frequency vector Ω_0 of the progenitor orbit is shown with an arrowed black line. The stream is slightly misaligned with Ω_0 ; the dashed line is a straight line fit to the positions of the test particles, and clearly demonstrates this misalignment. Also plotted with a red solid line is the image in angle-space of a circle in action-space, mapped by \mathbf{D} . The shape and orientation of the image reflects the λ_n and $\hat{\mathbf{e}}_n$ of \mathbf{D} for this orbit. The ellipse is clearly misaligned with the underlying orbit, but is perfectly aligned with the stream particles.

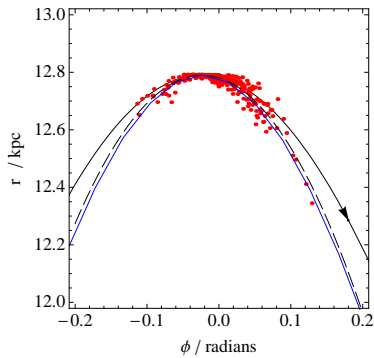


Figure 5. Real-space configuration for the stream of test particles shown in Fig. 4, plotted in polar coordinates. The arrowed black line shows the trajectory of the progenitor orbit. The stream formed by the dots falls away in radius faster than does the orbit, in both forwards and backwards directions: the stream clearly does not follow the progenitor orbit. The dashed line is a quadratic curve least-squares fitted to the stream, which shows that the stream has a substantially greater curvature than does the underlying orbit. The solid blue line is the track predicted by mapping the dashed line from Fig. 4 into real-space: it agrees perfectly with the stream.

the stream adequately. Thus, the small misalignment in angle-space is manifest as a significant change in stream curvature at apocentre.

Since we know the orientation of the long axis of the angle-space distribution for this stream, we can predict the stream track in real-space. The blue line in Fig. 5 shows the mapping into real-space of the dashed line from Fig. 4. The mapping is done by solving numerically for the real-space roots of the equations that relate action-angle variables to real-space coordinates: for spherical potentials, the appropriate equations are given in §3.5.2 of BT08. Fig. 5 shows that, unlike the progenitor orbit, this mapped line delineates the stream perfectly.

Although we have only considered the unrealistic case of a stream formed from an isotropic cluster, we have nonetheless pro-

duced a stream which is misaligned from its progenitor orbit in both angle-space and real-space.

We conclude that, in the isochrone potential, the track of the stream makes a poor proxy for the orbit of its stars, and that in general, streams in this potential cannot be relied upon to delineate orbits.

5 MAPPING STREAMS FROM ACTION-ANGLE SPACE TO REAL SPACE

The example of Fig. 5 shows that an angle-space misalignment can alter the curvature of the real-space stream. In this section, we examine why this is so, and show the range of real-space effects that are a consequence of angle-space misalignment. We will also examine the effects of a finite action-space distribution on the real-space track of a stream.

5.1 Non-isotropic clusters

Up until this point, we have considered our streams to form from a cluster of particles that is isotropic in \mathbf{J} , resulting in a stream that is perfectly aligned in angle-space with the principal direction of \mathbf{D} .

It is not obvious that this is a fair assumption. The structure in angle-space, given by equations (8) and (9), is linearly dependent upon the action-space distribution that generates it. By properly choosing that distribution, we can create streams of arbitrary shape in angle-space. Nature does not create clusters with arbitrary action-space distributions, so arbitrary-shaped streams do not emerge. But what kind of action-space distribution should be considered reasonable?

In Section 6 below, we will investigate the action-space distribution of real clusters, by means of N-body simulation. Here, we only require a qualitative understanding, in order to know what kind of gross action-angle structures we should learn to map. Since the action-space distribution fundamentally arises from the random motion of stars within the cluster, it is unlikely to be dominated by complex structure. We will therefore assume that the gross structure is ellipsoidal. But what should be the axis ratio of this ellipse?

Consider a cluster with isotropic velocity dispersion, σ , that is on an orbit with apocentre r_a and pericentre r_p , where it is tidally disrupted. In our spherical system, the radial action is given by the closed integral

$$J_r = \frac{1}{2\pi} \oint p_r dr, \quad (28)$$

where the integration path is one complete radial oscillation. Now consider a particle whose radial momentum p_r differs from that of the cluster average by $\delta p_r \sim \sigma$. We can take a finite difference over equation (28) and thus obtain an expression for the difference in radial action between the particle and the cluster

$$\delta J_r \sim \frac{1}{\pi} \delta p_r \Delta r \sim \frac{1}{\pi} \sigma \Delta r, \quad (29)$$

where $\Delta r = (r_a - r_p)$ is the amplitude of the radial oscillation. Now consider another particle, whose azimuthal velocity differs from that of the cluster by $\delta v_t \sim \sigma$. The difference in angular momentum between this particle and the cluster is

$$\delta L \sim r_p \delta v_t \sim r_p \sigma, \quad (30)$$

where we have performed our calculation at pericentre, because that is where the cluster is stripped. For the purposes of this section,

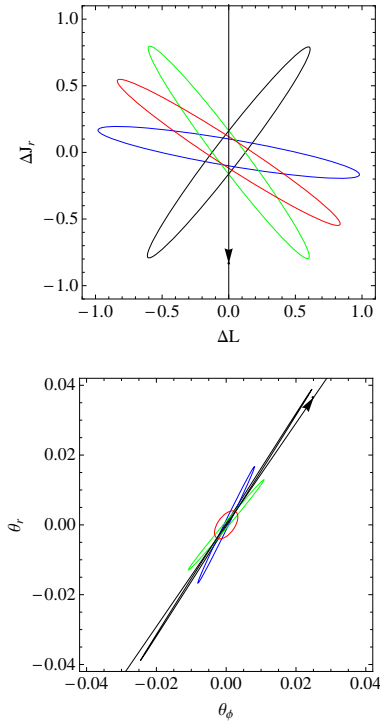


Figure 6. The upper panel shows a selection of ellipses in action-space, each of axis ratio 10, but oriented in different directions. The lower panel shows the image in angle-space that results from mapping each of the action-space ellipses with the linear map \mathbf{D} , calculated for the orbit II in the isochrone potential of Section 4.3.1. In the lower panel, the arrowed black line is the frequency vector Ω_0 ; in the upper panel, the arrowed black line is the inverse map of the frequency vector, $\mathbf{D}^{-1}\Omega_0$. We see that regardless of the shape in action-space, the mapped images are all elongated and roughly aligned with the orbit, although the alignment is generally not perfect. In this example, the misalignment of each of the red and green images is about 10 deg.

we are interested in the relative size of the spread in radial action ΔJ_r and the spread in angular momentum ΔL for a disrupting cluster. We see that their quotient

$$\frac{\Delta J_r}{\Delta L} \sim \frac{\Delta r}{\pi r_p}. \quad (31)$$

Although this ratio will take on every value between $(0, \infty)$ as we move from a circular orbit to a plunging one, for the orbits likely to be occupied by stream-forming clusters, it will typically be within an order-of-magnitude of unity.

The upper panel of Fig. 6 shows a set of ellipses, with axis ratio 10, placed at various orientations in action-space: an axis ratio of 10 would not be considered untypical by the arguments of the previous paragraph. The lower panel of Fig. 6 shows the images under \mathbf{D} of these ellipses in angle-space when evaluated on orbit II in the isochrone potential of the previous section. All the images are both elongated and roughly oriented towards the principal direction. We conclude that the images of most action-space ellipses under this map—and thus, most streams formed in this potential—would be highly elongated and oriented to within a few degrees of the principal direction, which is itself oriented to within a few degrees of the frequency vector Ω_0 .

Since the ratio of the eigenvalues for this orbit is ~ 17 , it is not possible to produce an image in angle-space that is not elon-

gated towards the principal direction, by mapping an action-space ellipse of axis-ratio 10. We note from Fig. 3 that, for this potential, the ratio of eigenvalues does not vary much, and nor does the principal direction stray from Ω_0 by more than a few degrees. We therefore conclude that reasonable action-space distributions will always result in the formation of streams in this potential, and that such streams will always be oriented in angle-space to within a few degrees of Ω_0 .

5.2 The mapping of action-angle space to real space

The upper-left panel of Fig. 7 shows three trajectories in angle space. The black line is the trajectory of II in the isochrone potential given in Section 4.3.1. The red line has a frequency ratio Ω_r/Ω_ϕ that is 10 per cent lower than the black line, and is therefore rotated from it by ~ 2.9 deg. Conversely, the blue line has a frequency ratio that is 10 per cent higher than the black line, and is therefore rotated from it by ~ 2.5 deg.

The red and blue lines were chosen to represent likely streams in angle-space that could form in the isochrone potential, given the results of the previous section. We note that the red line has retarded radial phase (relative to the black line) on the leading tail, and advanced radial phase on the trailing tail. Conversely, the blue line has advanced radial phase in the leading part, and retarded radial phase in the trailing part.

How do these lines map into real-space? The upper-right panel of Fig. 7 shows the real-space curve obtained from the lines in the upper-left panel of that figure, having chosen the point of intersection such that the lines are phase-matched near apocentre. The curves in the upper-right panel have been drawn by assuming that all points along each line have the same \mathbf{J} . Thus, this plot represents the real-space curves of streams oriented in angle-space according to the upper-left panel, but formed from clusters of vanishingly small $\Delta \mathbf{J}$.

In the upper-right panel, we see that the red line has systematically lower curvature than the black line. Conversely, the blue line has systematically greater curvature than the black line. This is because the red curve has retarded radial phase on the leading tail, and advanced radial phase on the trailing tail, and thus is flattened with respect to the orbit. Similarly, the blue line has advanced radial phase on the leading tail, and retarded radial phase on the trailing tail, and thus appears curved with respect to the orbit.

The lower-left panel of Fig. 7 shows the same lines, but now phase-matched at pericentre. Similarly to the upper-right panel, the red line again appears less curved with respect to the orbit, and the blue line appears more curved with respect to the orbit. The lower-right panel of that figure also shows the same lines, phase-matched at a point well away from apsis. In this case, a misalignment between the stream and Ω_0 in angle-space manifests itself as a real-space directional misalignment, rather than a curvature error as at apsis. This occurs because, unlike at apsis, the mapping between angle-space and real-space plane polar coordinates is relatively undistorted near this point.

In summary, realistic angle-space distributions in an isochrone potential, which may be misaligned with the progenitor frequency by a few degrees, will produce real-space streams that exhibit differing curvature from the progenitor orbit when observed at apsis, and differing directional alignment from the orbit when observed far away from apsis.

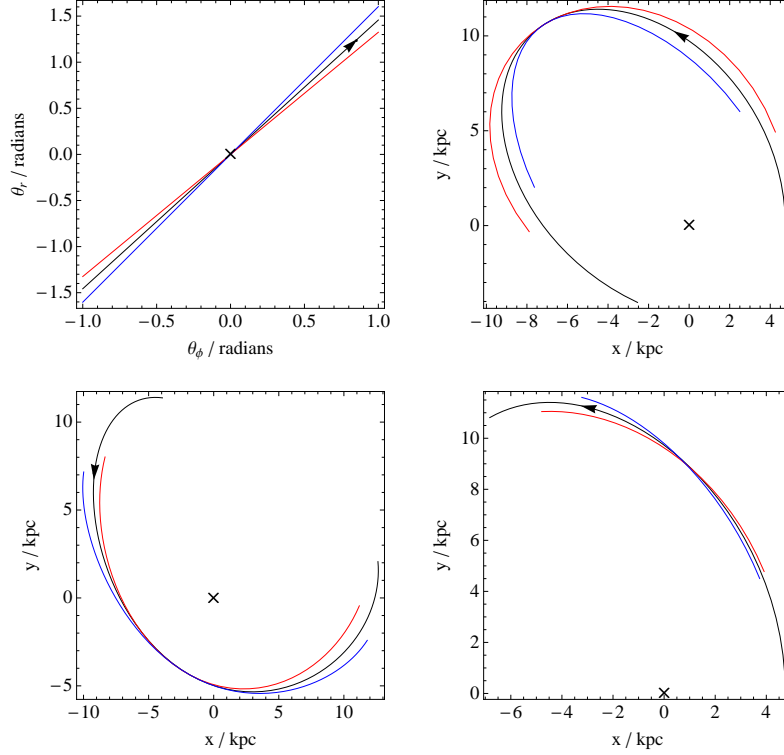


Figure 7. The upper-left panel shows three trajectories in angle space. The black line is the trajectory of orbit I1 in the isochrone potential of Section 4.3.1. The red line has a frequency ratio Ω_r/Ω_ϕ that is 10 per cent lower than I1. The blue line has a frequency ratio that is 10 per cent higher than I1. The lines are phase-matched at their point of intersection. We note that the red line has retarded radial phase (relative to the black line) on the leading tail, and advanced radial phase on the trailing tail. Conversely, the blue line has advanced radial phase in the leading part, and retarded radial phase in the trailing part. The other three panels show the real-space images of these three lines, when phase-matched: (upper-right) near apocentre, (lower-left) near pericentre, and (lower-right) at a point far from apsis. In each of these three panels, the centroid of the potential is marked with a cross.

5.3 Are trajectories insensitive to small changes in \mathbf{J} ?

To this point, all real-space tracks have been derived from streams in angle-space under the assumption that at all points along that stream the action is that of the progenitor, \mathbf{J}_0 . This assumption is only strictly valid in the case of a vanishingly small action-space distribution, and for asymptotically large time since disruption of the cluster. If a mapping into real-space from a line in angle-space is made under this assumption, then a stream generated by a sufficiently broad action-space distribution will not be accurately represented, even though the representation in angle-space may be exact. This is because the small changes in action that give rise to the small changes in frequency also cause small changes in real-space trajectory as well.

When computing a stream track in real-space, it is possible to correct for this effect. By inverting equation (9) and eliminating $\Delta\Omega$ using equation (8), we find that for a star separated from a fiducial point on the stream by angle $\delta\theta$, the difference in action between the star and the fiducial point, $\delta\mathbf{J}$ is given by

$$\delta\mathbf{J} = \frac{1}{t_d} \mathbf{D}^{-1} \delta\theta, \quad (32)$$

where t_d is the time since the star and the fiducial point were coincident. We may therefore guess the correction $\delta\mathbf{J}$ for a star's true action ($\mathbf{J}_0 + \delta\mathbf{J}$) from its position in the stream, provided we know t_d .

We typically take the fiducial point to be the centroid of the stream, following which we may assume t_d to be the time since

the first pericentre passage of the cluster on its present orbit. Although this assumption neglects the possibility that the star could have been torn away during a subsequent pericentre passage, we note that during tidal disruption, it is the fastest moving stars which become unbound. The cluster core that remains after a pericentre passage therefore has lower velocity dispersion. Stars subsequently torn from that cluster will therefore have a smaller distribution in action-space. Consequently, the stars with the largest $\delta\theta$ from the centroid—i.e. those for which the $\delta\mathbf{J}$ correction will be most important—must have been torn away at the earliest time, and so the assumption that t_d equals the time since the first pericentre passage remains good.

Just how important is this effect? For small changes in J_r , the trajectory changes we discuss are expressed as changes in the radial amplitude Δr , while the guiding-centre radius r_g , which is purely a function of L , is held constant. We can estimate the magnitude of the effect as follows.

Consider a cluster on an orbit that is close to circular, whose radial action is given by equation (28). Orbital energy E is conserved, so close to apsis $r = r_0$, the radial momentum p_r is given by

$$\begin{aligned} E &= \frac{1}{2} p_r^2(r) + \Phi_{\text{eff}}(r) \\ &\simeq \frac{1}{2} p_r^2(r) + \Phi_{\text{eff}}(r_0) + (r - r_0) \left. \frac{d\Phi_{\text{eff}}}{dr} \right|_{r_0}, \end{aligned} \quad (33)$$

where we have defined the effective potential

$$\Phi_{\text{eff}}(r) = \Phi(r) + L^2/2r^2. \quad (34)$$

Since at apsis $p_r = 0$,

$$E = \Phi_{\text{eff}}(r_0). \quad (35)$$

Hence from equation (33) we have

$$p_r(r) = \sqrt{-2(r-r_0) \left. \frac{d\Phi_{\text{eff}}}{dr} \right|_{r_0}} = \sqrt{2(r-r_0)F_{\text{eff}}(r_0)}, \quad (36)$$

where we have defined the effective force,

$$F_{\text{eff}}(r') = -\partial\Phi_{\text{eff}}/\partial r|_{r'}. \quad (37)$$

If (r_a, r_p) are apocentre and pericentre respectively, then

$$p_r(r) \simeq \begin{cases} \sqrt{2|F_{\text{eff}}(r_a)|(r_a-r)} & \text{if } r \simeq r_a, \\ \sqrt{2|F_{\text{eff}}(r_p)|(r-r_p)} & \text{if } r \simeq r_p. \end{cases} \quad (38)$$

Hence, we define a global approximation to p_r

$$\tilde{p}_r(r) = \frac{\sqrt{2|F_{\text{eff}}|(r-r_p)(r_a-r)}}{\sqrt{\Delta r}}, \quad (39)$$

where $\Delta r = r_a - r_p$ and F_{eff} a constant set equal to the value of $F_{\text{eff}}(r)$ at either apsis, since we assume it takes approximately the same value at both. We note that

$$\int_{r_p}^{r_a} \sqrt{(r-r_p)(r_a-r)} dr = \frac{\pi}{8} \Delta r^2, \quad (40)$$

so when combined with equation (39), equation (28) for J_r yields

$$J_r = \frac{1}{8} \sqrt{2|F_{\text{eff}}| \Delta r^3}. \quad (41)$$

We can deduce the value of F_{eff} as follows. We note that

$$\Phi_{\text{eff}} = \Phi + \frac{L^2}{2r^2}, \quad (42)$$

and that its derivative is

$$\frac{d\Phi_{\text{eff}}}{dr} = \frac{d\Phi}{dr} - \frac{L^2}{r^3}. \quad (43)$$

If the rotation curve is relatively flat, then $F_{\text{eff}}(r)$ evaluated at $r_a \simeq r_g + \Delta r/2$ is

$$\begin{aligned} F_{\text{eff}} &= \left. \frac{d\Phi_{\text{eff}}}{dr} \right|_{r_a} = \frac{v_c^2}{r} - \frac{L^2}{(r_g + \frac{1}{2}\Delta r)^3} \\ &\simeq \frac{v_c^2}{r_g} \left(1 - \frac{\Delta r}{r_g}\right) - \frac{L^2}{r_g^3} \left(1 - \frac{3}{2} \frac{\Delta r}{r_g}\right) \\ &= -\Delta r \left(\frac{v_c^2}{r_g^2} + \frac{3L^2}{2r_g^4} \right) = -\frac{5v_c^4 \Delta r}{2L^2}, \end{aligned} \quad (44)$$

and similarly when evaluated at r_p , but with opposite sign. Equation (41) then becomes

$$J_r \simeq \frac{\sqrt{5}v_c^2 \Delta r^2}{8L}. \quad (45)$$

Differentiating the above expression, we find

$$\begin{aligned} \frac{dJ_r}{d\Delta r} &= \frac{\sqrt{5}v_c^2 \Delta r}{4L} \\ &= \sqrt{\frac{5J_r v_c^2}{2L}}. \end{aligned} \quad (46)$$

Hence, for a small change δJ_r we can estimate the corresponding change in the radial amplitude, $\delta \Delta r$, which is likely to be a good

estimate for the positional error we would make in assuming that a star with action $J_r + \delta J_r$ actually had action J_r .

We can confirm the predictions of the above equations numerically. The left panel of Fig. 8 shows the real-space trajectory of the circular orbit I2, with radius $r = 8$ kpc, in the isochrone potential of Section 4.3.1. Also plotted is the trajectory of an orbit that has identical L to I2, but $J_r = 0.21 \text{ km s}^{-1} \text{ kpc}$.

Clearly, equation (46) ceases to have meaning when faced with orbits very close to circular, so we rely for our estimate on the integral form equation (45) instead. Equation (45) predicts $\Delta r = 0.16$ kpc for this perturbation from circular, which appears from the left panel of Fig. 8 to be a reasonable estimate.

From equation (46) we see that the magnitude of the effect diminishes with increasing J_r as $\delta \Delta r \sim 1/\Delta r \sim 1/\sqrt{J_r}$. The centre panel of Fig. 8 shows this to be the case. The panel shows two trajectories in the isochrone potential: one for the orbit I3, and one for the same orbit with J_r incremented by 0.1 per cent. Equation (46) predicts a change $\delta \Delta r \sim 3$ pc. Close inspection of the trajectories confirms an actual $\delta \Delta r \sim 3$ pc, so the prediction is correct, but as is clear from Fig. 8, corrections of such magnitude are negligible.

What follows is an estimate for the positional error made by incorrectly guessing L . Consider again a cluster on an orbit close to circular. The angular momentum of the cluster is related to the guiding-centre radius r_g and the circular velocity v_c by

$$L = v_c r_g. \quad (47)$$

Consider now a star whose angular momentum is suddenly reduced by δL . This star is now at apocentre, since its guiding-centre radius has been reduced by

$$\delta r_g = \frac{\delta L}{v_c}, \quad (48)$$

where we have assumed that the rotation curve is flat. The pericentre radius will have been reduced by of order twice the change in guiding-centre radius, hence we may write

$$\delta \Delta r = \frac{2\delta L}{v_c}. \quad (49)$$

Thus, we can predict the change in radial amplitude $\delta \Delta r$ for a small change in angular momentum δL , which is likely to be a good estimate for the positional discrepancy we would encounter in assuming that a star with angular momentum $L + \delta L$ actually had angular momentum L .

Again, we can check the predictions of this expression numerically. The right panel of Fig. 8 shows the trajectories of two orbits in our isochrone potential. The red line is orbit I2, while the black line is the same orbit, but with the angular momentum increased by 1 per cent. Equation (49) predicts $\Delta r \simeq 0.16$ kpc for this change. Fig. 8 shows that this estimate is close to exact.

The only example we have considered thus far for which this effect could be of consequence is the isochrone-potential stream shown in Fig. 5. For this cluster, equation (46) predicts that a positional error of ~ 2 pc would be accrued by assuming all stars have the same radial action. Similarly, equation (49) predicts that a positional error of ~ 1.5 pc will be accrued by assuming that all stars have the same angular momentum. These errors are insignificant, so no corrections are required in this case.

However, the scale of the $\Delta \mathbf{J}$ distribution in the example of Fig. 5 was deliberately chosen to be very small, with a velocity dispersion $\sigma \sim 4 \times 10^{-2} \text{ km s}^{-1}$. The equations (46) and (49) show the magnitude of the trajectory anomaly rises linearly with the scale of $\Delta \mathbf{J}$. For a large cluster with $\sigma \sim 20 \text{ km s}^{-1}$ on the

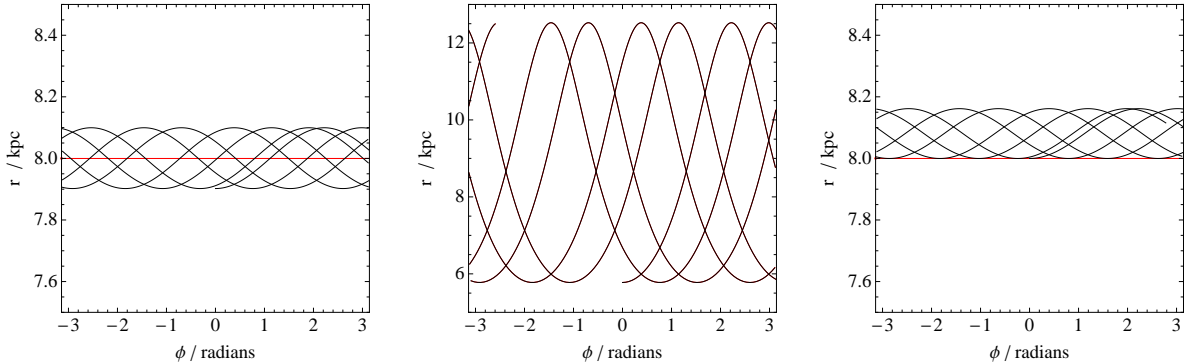


Figure 8. The effect of small changes in actions on real-space orbital trajectories. The left panel shows that a small change in J_r ($\delta J_r = 0.21 \text{ km s}^{-1} \text{ kpc}$) to a circular orbit (I2 in Table 1 shown in red) produces a change of $\delta \Delta r \sim 0.2 \text{ kpc}$ in radial amplitude. The centre panel shows the effect of the same perturbation δJ_r on an eccentric orbit (I3 in Table 1) with the same angular momentum as the circular orbit, but with $J_r = 207 \text{ km s}^{-1} \text{ kpc}$. The effect on radial amplitude is so small as to be invisible in this plot. The right panel shows the effect of an increment in angular momentum L of 1 per cent on the trajectory of the orbit I2. In this case, the radial amplitude changes by $\delta \Delta r \sim 0.15 \text{ kpc}$.

orbit I2, this would imply trajectory errors of order $\sim 1 \text{ kpc}$, which are not negligible. Therefore, consideration of the effects of a finite action-space scale on the real-space track of streams is necessary in practical cases.

In the case of a large cluster, even a stream that is perfectly aligned with its frequency vector in angle-space will not be delineated by the progenitor orbit in real-space. The correction described by equation (32), to account for variation in action down the stream will be required to correctly predict the stream-track from its angle-space distribution. In general we would not know the time since first pericentre t_d accurately, although given \mathbf{J}_0 and a knowledge of the extent of the stream, we could make a reasonable guess as to its value. However, even a poor, but finite, guess for the value of t_d would likely produce a more accurate real-space stream track than would assuming $\mathbf{J} = \mathbf{J}_0$ everywhere along the stream.

6 THE ACTION-SPACE DISTRIBUTION OF DISRUPTED CLUSTERS

To this point, we have relied upon the qualitative estimate from Section 5.1 for what the action-space distribution of a disrupted cluster might be. In this section, we investigate the action-space distribution of various cluster models using N-body simulation. We further utilize our N-body models to confirm the misalignment between streams and orbits, and to demonstrate that we can accurately predict the real-space track of the stream.

The action-angle coordinates, of the host-galaxy potential, have limited usefulness when applied to the particles in a bound cluster, because the actions are not constant with time. Nonetheless, they remain a valid set of canonical coordinates and can be legitimately used to describe the phase-space distribution of the cluster. Moreover, we shall see that a disrupted cluster gives rise to a characteristic distribution in action-space, from which the track of the stream can be predicted.

Fig. 9 shows a segment of each of the orbits I4 and I5 in the isochrone potential of Section 4.3.1. These orbits were chosen to be fairly representative of those occupied by tidal streams in our Galaxy: they have apocentre radius $\sim 20 \text{ kpc}$ and are moderately eccentric to allow for efficient tidal stripping. For our investigation, we wish to launch model clusters on each of these orbits, where the otherwise-stable cluster has been chosen such that its outermost

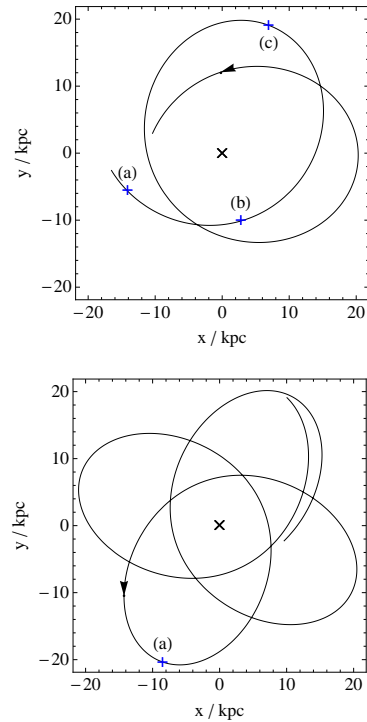


Figure 9. Plan views of the orbits used in this section. The top panel shows I4, with (a), (b) and (c) marking the positions of the cluster corresponding to the upper-left, upper-middle and upper-right panels of Fig. 10 respectively. The bottom panel shows I5, with (a) marking the position of the cluster corresponding to the bottom-right panel of Fig. 12. In both panels, the potential in use was the isochrone potential described in Section 4.3.1.

stars will be torn away by tidal forces when close to pericentre. The process by which we choose our model clusters is detailed in the next section.

6.1 Cluster models

We work with King models (King 1966, BT08) for our clusters, since these simple models are both easy to generate and are fairly

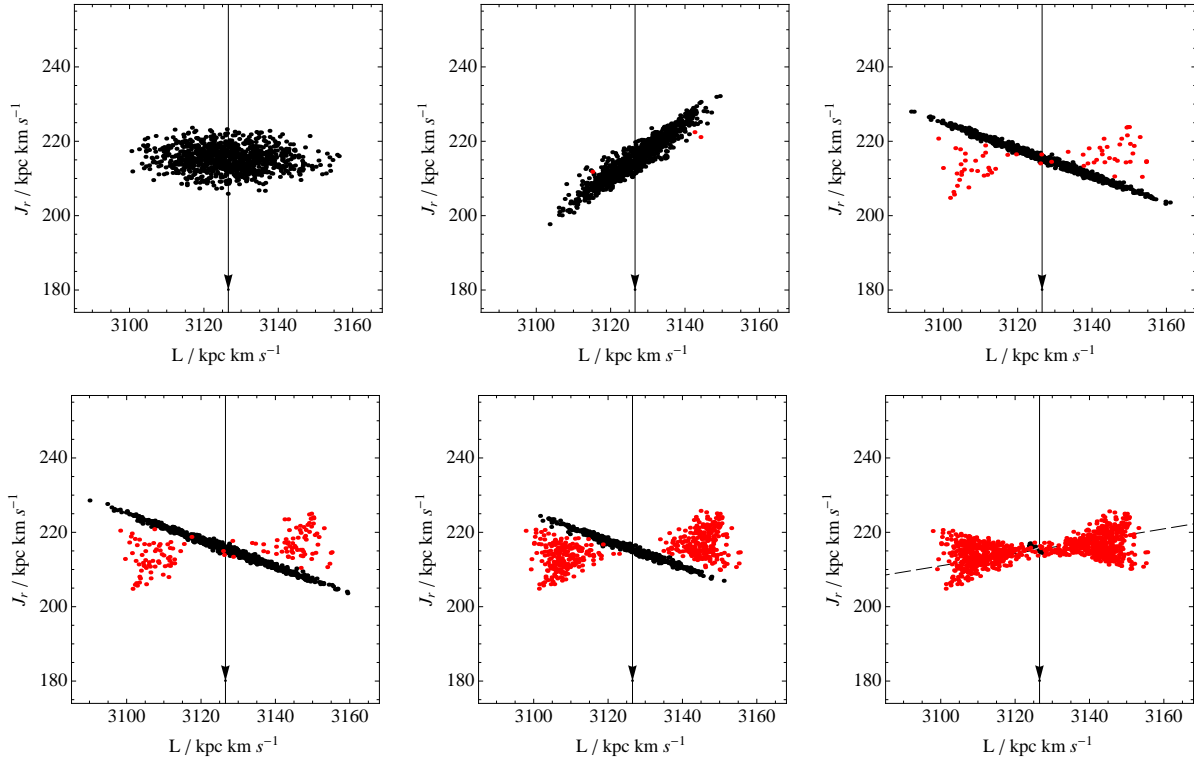


Figure 10. The action-space distribution of particles for the N-body cluster model C1, at different times along the orbit I4. From left-to-right and top-to-bottom, these times are: shortly after release; first pericentre passage; first apocentre passage; second apocentre passage; 7th apocentre passage; 14th apocentre passage. The solid black line is the inverse map of the frequency vector, $\mathbf{D}^{-1}\boldsymbol{\Omega}_0$. The dashed line in the bottom-right panel represents a least-squares linear fit to the particle distribution.

representative of some observed globular cluster profiles (Fig. 6.18, Binney & Merrifield 1998). The profile of a King model can be defined by $W \equiv \Phi_0/\sigma^2$, the ratio of the central potential to the squared-velocity parameter σ^2 . For a given W , all resulting models are similar in terms of $\rho(\tilde{r}/\tilde{r}_0)/\rho_0$, where ρ_0 is the central density and \tilde{r}_0 is the core radius. An exact model is specified by choosing ρ_0 and \tilde{r}_0 , in addition to W , either directly or through a relation with another parameter.

For a given orbit, we specify our models as follows. Following the argument of Dehnen et al. (2004), we note that a cluster of mass M_c orbiting at a galactocentric radius r from the centre of a host galaxy with circular velocity v_c , will be tidally pruned to the cluster radius \tilde{r}_{tide} , where

$$\tilde{r}_{\text{tide}}^3 \simeq \frac{GM_c}{v_c^2} r^2. \quad (50)$$

We freely choose a profile parameter W and a cluster mass M_c , and we also specify a galactocentric stripping radius $r_s > r_p$, where r_p is the pericentre radius of the orbit concerned. We then set \tilde{r}_t , the cluster truncation radius, equal to \tilde{r}_{tide} from equation (50), where $r \rightarrow r_s$ and $v_c \rightarrow v_c(r_s)$. The resulting cluster will remain intact while $r \gg r_s$, but will have its outermost stars tidally stripped when $r \sim r_p$.

6.2 The disruption of a cluster

The low-mass cluster model C1 (Table 3) was specified for the orbit I4 (Table 1) according to the schema in Section 6.1. We chose a low value $W = 2$ for the profile parameter of for our basic cluster

model, in order to ensure the presence of many particles near the cluster truncation radius \tilde{r}_t during successive stripping events.

A 10^4 particle realization of the cluster model C1 was made by random sampling of the King model distribution function (equation 4.110 of BT08). This cluster was placed at a point shortly after apocentre on the orbit I4 in the isochrone potential of Section 4.3.1. The cluster was evolved forward in time in the aforementioned potential by the FVFPs tree code of Londrillo et al. (2003), using a time step of $dt = t_{\text{dyn}}/100$ and a softening length ϵ as specified in Table 3. The simulated time period was 4.81 Gyr, or almost 14 complete radial orbits.

Fig. 10 shows the evolution of the action-space distribution of the cluster model C1 as a function of time. In all the panels of that figure, an arrowed black line shows the mapping of the frequency vector from angle space into action space, $\mathbf{D}^{-1}\boldsymbol{\Omega}_0$. This vector indicates the direction that maps onto $\boldsymbol{\Omega}_0$ in angle-space, so any action-space distribution that is aligned with this vector will be aligned with $\boldsymbol{\Omega}_0$ in angle-space.

In all cases involving the isochrone potential, $\mathbf{D}^{-1}\boldsymbol{\Omega}_0$ is oriented exactly along the J_r axis. We can understand this from equation (26), which shows that in the isochrone potential, the frequency direction $\boldsymbol{\Omega}_0$ is a function of L only, and is independent of J_r . Thus, a line of constant $\hat{\boldsymbol{\Omega}}_0$ must map into action-space as a line of constant L . This is a peculiar feature of the isochrone potential, and is not true for a general potential.

The upper-left panel of Fig. 10 shows the configuration of the cluster immediately after release, at position (a) in the upper panel of Fig. 9. The distribution is ellipsoidal without additional sub-structure, which we expect since the distribution in action results

Table 3. Details of the cluster models used in this section. The defining parameters for each model are (W, M_c, r_s) , while $(r'_{\text{lim}}, \sigma, t_{\text{dyn}}, \epsilon)$ are derived parameters.

	W	M_c	r_s	r'_{lim}	σ	t_{dyn}	ϵ
C1	2	$10^4 M_\odot$	12 kpc	48.6 pc	1.18 km s^{-1}	12.6 Myr	1.0 pc
C2	2	$10^5 M_\odot$	12 kpc	104.8 pc	2.54 km s^{-1}	12.6 Myr	2.2 pc
C3	6	$10^4 M_\odot$	12 kpc	48.6 pc	1.14 km s^{-1}	2.36 Myr	0.32 pc
C4	2	$10^4 M_\odot$	11 kpc	45.5 pc	1.22 km s^{-1}	11.79 Myr	0.94 pc
C5	2	$10^4 M_\odot$	11 kpc	45.7 pc	1.22 km s^{-1}	11.79 Myr	0.94 pc

entirely from the approximately spheroidal density profile, and the approximately isotropic velocity dispersion, of the cluster. We understand the ellipticity of the action-space distribution from Section 5.1. Indeed, the prediction of equation (31) of $\Delta J_r / \Delta L \sim 0.3$ for this orbit can be seen to be approximately correct.

In the upper-middle panel of Fig. 10, the cluster has now moved from its point of release to its first pericentre passage, marked as position (b) in Fig. 9. We see that the ellipse has flattened somewhat, and has rotated anticlockwise. In the upper-right panel, the cluster has now progressed to the subsequent apocentre passage, marked as position (c) in Fig. 9. Here, the cluster is again flattened, but now it has rotated clockwise.

We can qualitatively understand this behaviour as follows. Consider a particle in a cluster near apsis. What changes to the actions will be made by perturbations to the velocity of this particle? A perturbation δv to the transverse velocity will cause a change to the angular momentum

$$\delta L = r \delta v. \quad (51)$$

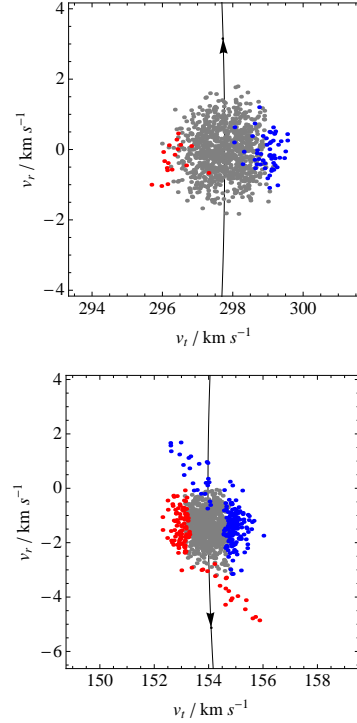
By means of the mechanism described by equation (49), this δL will cause a change in the guiding-centre radius r_g , which will cause a corresponding change in the radial action, according to equation (46). Conversely, a perturbation to the radial velocity will cause negligible change to the radial action, since

$$\delta E \simeq p_r \delta p_r = \dot{r} \delta v \sim 0, \quad (52)$$

and $J_r(E, L)$ remains unchanged. Hence, the distribution in both J_r and L is governed primarily by the transverse velocity when the cluster is at apsis, and the high degree of correlation observed in Fig. 10 reflects this.

We can confirm this analysis by examining Fig. 11. The upper panel shows (v_r, v_t) for the cluster near its first pericentre passage, while the lower panel shows the same for the cluster near its subsequent apocentre passage. The particles coloured red are those with $L < 3110 \text{ kpc km s}^{-1}$ and those coloured blue have $L > 3140 \text{ kpc km s}^{-1}$. The boundary between the colours is very sharp in the v_t direction, as one would expect, since the particles have been coloured on the basis of L . However, we note that particles with the full range of v_r contribute to both the blue and red regions equally, despite Fig. 10 showing that J_r is very different for these two regions. Hence J_r must be independent of v_r near apsis.

We complete our explanation of the orientation of the action-space distribution by taking note of the sign of the change in J_r near apsis. Increasing L will always increase r_g , and when the cluster is at pericentre, this pushes r_g further away, and so increases the radial action. Conversely, when the cluster is at apocentre, increasing r_g brings it closer to the cluster, and so decreases the radial action. Thus, we see that near pericentre, particles with high L will have high J_r and the distribution will be rotated to have a positive gradient $\Delta J_r / \Delta L$. Conversely, at apocentre, particles with high L

**Figure 11.** Radial velocity versus tangential velocity for the C1 cluster model, on the I4 orbit, at (top panel) the first pericentre passage, and (bottom panel) the first apocentre passage.

will have low J_r , and so the distribution will be rotated to have a negative gradient $\Delta J_r / \Delta L$.

We can predict the value of the gradient of this distribution, by combining equation (46) and equation (49). We find

$$\frac{dJ_r}{dL} \sim \pm \sqrt{\frac{2\sqrt{5}J_r}{L}}, \quad (53)$$

where the sign of the radical depends on the apsis under consideration, as detailed above. We can see from the upper-right panel of Fig. 10 that this equation predicts approximately the correct gradient of $dJ_r/dL \sim -0.5$, when evaluated for the orbit I4. We further note that this equation implies that the gradient will be steeper for an orbit of greater eccentricity.

Let us again examine Fig. 10, and note that the black particles are those still bound to the cluster, while the red particles are those that are unbound, where we have defined ‘bound’ to mean all particles that are within r_{tide} of the cluster barycentre. In the upper-right plot, which shows the cluster configuration at the first apocentre passage, the few unbound particles form an approximately horizontal distribution. These are particles that have been stripped from the

cluster near to the preceding pericentre passage, which is depicted in the upper-middle panel of Fig. 10.

We note two things. First, the bulk of the stripped particles have large ΔJ from the cluster centroid; this is simply a consequence of the high-speed stars being most likely to be stripped. Second, we note that although the red particles in the upper-right panel span approximately the same range in L as the black particles in the upper-middle panel, they span a range in J_r that is only about half that spanned by the black particles.

We explain this as a result of the cluster’s self-gravity, as follows. Particles that are stripped from the cluster mostly escape through the Lagrange points L_1 and L_2 . These two points lie near the cluster along the line from the barycentre of the host to the cluster (Fig. 8.6 of BT08). Thus, it is the particles’ radial velocity which initially carries them away from the cluster, and it is from this velocity component that the particles pay most of the energetic penalty for escaping, with the consequence that the radial velocity dispersion of the escaping stars is reduced. This reduction in the radial velocity dispersion corresponds to a compression in J_r of the distribution of escaping particles. Once unbound, the particles are carried further away from the cluster along a complex trajectory that ends up with the now-free particle drifting away from the cluster according to the mapping in equation (8). Thus, the final sum of the energetic penalty is paid from the difference in action $\mathbf{J} - \mathbf{J}_0$ between the particle and the cluster, with the net result that the unbound distribution uniformly shrinks. The latter effect is minor compared to the compression in J_r , because much more work is done in becoming unbound than in escaping to infinity once already unbound. The complete effect is to generate an unbound distribution, that looks like the high ΔJ wings of the pericentre distribution, but is compressed in J_r and slightly shrunk.

Looking again at Fig. 10, we note that in the lower-middle panel, which corresponds to the 7th apocentre passage, many particles have escaped, and the size of the bound distribution has visibly shrunk. We understand this as a consequence of the most energetic particles having already escaped the cluster, leaving behind a colder core. By the time of the 14th apocentre passage, shown in the lower-right panel, almost all the particles have escaped. We note that the positions of many of the red particles have remained static between the lower-middle and lower-right panels. The action-space distribution of the unbound particles is therefore frozen in place, confirming that self-gravity is unimportant after a stream has initially formed.

In conclusion, we have qualitatively understood the distortion of a cluster in action-space as it passes through pericentre and apocentre along its orbit. We have found that stars stripped at pericentre form a distribution that is derived from the pericentre distribution of bound stars, but is compressed in J_r . We have found that the pericentre distribution exhibits a high correlation between J_r and L , and that the gradient of this correlation in (L, J_r) scales as $\sim \sqrt{J_r/L}$. We typically assume that our cluster orbit will have large L and comparatively smaller J_r : this would only be untrue for extreme plunging orbits, which are not likely to be relevant to the problem in hand. Hence the gradient in (L, J_r) will typically be less than unity, and the compression will only act to shrink it still further: the stripping mechanism produces an action-space distribution that is both flattened and very roughly oriented along \hat{L} .

6.2.1 The effect of changing the cluster model or orbit

We now investigate the qualitative effects on the action-space distribution of a disrupted cluster of changing the cluster model param-

eters, or the cluster orbit. The cluster models used in this section are C1 to C4, detailed in Table 3. These clusters were created according to the schema of Section 6.1, taking the orbit to be I4 in the isochrone potential of Section 4.3.1 for the models C1–C3, and taking the orbit to be I5 in the same potential for the model C4.

The cluster model C1, the evolution of which along the orbit I4 was detailed in the previous section, is used as our baseline to which we compare the distributions of the other clusters. The cluster model C2 has the same profile parameter, $W = 2$, as does C1, but is 10 times more massive. The result is a cluster that is both heavier and proportionately larger while being stripped at the same galactocentric radius, r_s .

The cluster model C3 has the same mass as does C1, but is considerably more concentrated, with a profile parameter $W = 6$. The cluster has an identical truncation radius \tilde{r}_t and velocity scale σ , but has significantly fewer particles near to \tilde{r}_t than C1. The particles of C3 are generally more tightly bound to the cluster than are those of C1.

The cluster model C4 has the same mass and profile parameter as C1, but is specified for the orbit I5, which has lower L than I4, and thus a smaller pericentre radius. The resulting cluster is slightly more compact, allowing it to survive to a closer galactocentric radius than can C1.

A 10^4 particle realization of each of the models C1–C3 was placed at a point shortly after apocentre on the orbit I4, and evolved forward in time by the FVFPS tree code, using a time step of $dt = t_{\text{dyn}}/100$ and a softening length ϵ as specified in Table 3. The total period of the simulation was 2.36 Gyr, or almost 7 complete radial orbits. Additionally, a 10^4 particle realization of C4 was placed at a point shortly after apocentre on the orbit I5, and evolved forward in time by the FVFPS tree code, for a total period of 2.21 Gyr, or almost 7 complete radial orbits.

Fig. 12 shows the action-space distribution for the cluster at the seventh apocentre passage, for each of these simulations. The top-left panel shows C1 on the orbit I4, and is identical to the lower-middle panel in Fig. 10. The top-right panel shows the cluster C2 on the same orbit; the bottom-left panel shows the cluster C3 on the same orbit; and the bottom-right panel shows the cluster C1 on the orbit I5.

In the top-right panel, we see that the action-space distribution of the more massive cluster is qualitatively identical to that of C1, except that the distribution has approximately twice the scale. We conclude that cluster mass merely sets the scale of distribution in action-space of stripped stars.

The bottom-left panel shows the distribution from the more centrally concentrated cluster C3. In this case, the region occupied by bound particles is longer than for C1, reflecting the greater internal random velocities of the more concentrated model. However, the gross structure of the unbound distribution is approximately the same as for C1. This is because the extent of this distribution is defined by the least bound stars, stripped from the outer parts of each cluster: the behaviour of these stars is determined only by the mass of the cluster, and not by its internal configuration. Thus we conclude that cluster concentration does not alter the general shape of the eventual action-space distribution.

The bottom-right panel shows the distribution from the cluster C4 on the orbit I5, which has the same apocentre radius as I4 but a pericentre radius about 33 per cent smaller. Unlike in the other panels, the cluster has become completely unbound by the 7th apocentre passage on I5, which is likely to be a result of $(r_s - r_p)$ being slightly larger for C4 on I5, when compared to the other clusters on I4, resulting in more efficient stripping at pericentre.

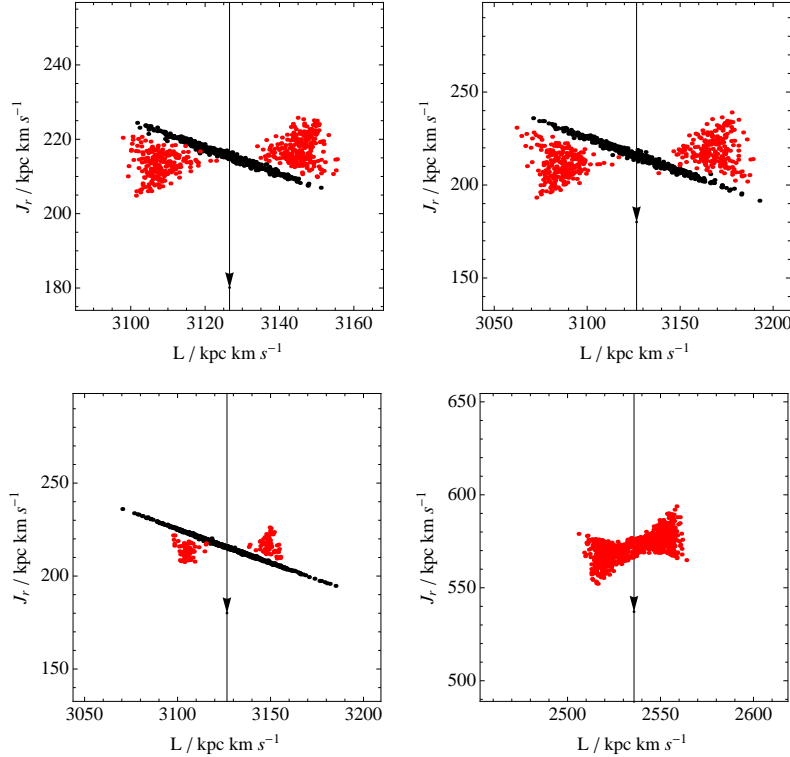


Figure 12. The action-space distribution of particles for cluster models on various orbits. Each plot shows the distribution at the 7th apocentre passage. Black points are bound to the cluster, red points orbit free in the host potential. From left-to-right and top-to-bottom, the panels show: the C1 cluster on the orbit I4; the C2 cluster on the orbit I4; the C3 cluster on the orbit I4; and the C4 cluster on the orbit I5. Note the change of scale between successive plots.

The distribution shown in this plot has approximately the same scale in ΔL as does the distribution from I4, but has approximately twice the scale in ΔJ_r . This is a consequence of the gradient dJ_r/dL given by equation (53) being steeper for I5 than for I4. Further, since we have already noted that this cluster was stripped faster than was C1, the energetic penalty for escaping must be lower, and so we expect less compression in J_r . The resulting distribution is similar to that of the top-left panel, but less compressed in the \hat{J}_r direction. Thus we conclude that changing the cluster orbit can distort the shape of the action-space distribution of unbound particles, but does not affect its basic structure.

6.3 Predicting the stream from the action-space distribution

We have determined the action-space distribution for several disrupted cluster models by means of N-body simulation. We now ask whether we can accurately predict the real-space path of the stream, given the action-space distribution of one of those models.

Suppose that we know the time t_d since a cluster’s first pericentre passage. The angle-space distribution is predicted by equation (8), where \mathbf{D} is evaluated on the progenitor orbit \mathbf{J}_0 and $t \rightarrow t_d$. We will use as an example the action-space distribution shown in the bottom-right panel of Fig. 10, which corresponds to the 14th pericentre passage of the simulated cluster C1 on the orbit I4. The upper panel of Fig. 13 shows the angle-space configuration corresponding to this panel: the grey particles are for angles directly computed from the results of the N-body simulation, while the red particles are for those predicted by equation (8), assuming t_d is known. Also plotted is the frequency vector Ω_0 , shown as a black arrowed line. The distributions of black and grey particles in

this panel agree perfectly. Furthermore, both distributions are obviously misaligned with the progenitor orbit.

The lower panel of Fig. 13 shows the real-space configuration of particles for the same scenario. The grey particles are again plotted directly from the results of the N-body simulation, while the red particles result from the mapping into real-space of the red particles from the upper panel. As in angle-space, the two distributions agree perfectly. Furthermore, the real-space manifestation of the misalignment of the stream with the orbit can be seen: the stream delineates a track that has substantially lower curvature than the orbit.

Our attempt to predict the real-space stream configuration from the action-space distribution has been completely successful. However, any complete model of the bottom-right panel of Fig. 10 must necessarily be rather complicated. It might not be possible to guess the form of this distribution without full N-body modelling. The dashed line in the bottom-right panel of Fig. 10 is a least-squares fit of the action-space distribution to a line. This represents a simpler model of the action-space distribution, which it might well be possible to guess *ab initio* for a cluster on a given orbit.

How good a prediction for the stream track can we get from this line? The blue lines in Fig. 13 show the results of mapping this line into both angle-space and then real-space. It is clearly an excellent fit to the stream, in marked contrast to the orbit, which is a much poorer model of the stream. Thus, even a very simple model of the cluster in action-space—albeit one deduced from an accurate knowledge of the distribution—allows us to predict stream tracks accurately.

Finally, we note that during the mapping of this line into real-

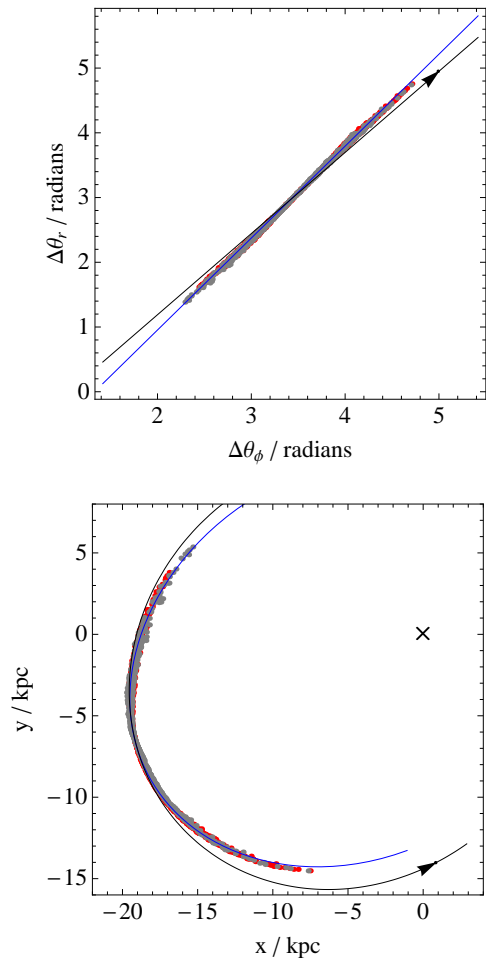


Figure 13. The distribution of particles for cluster C1, near its 14th apocentre passage on orbit I4. The upper panel shows the angle-space distribution, while the lower panel shows the configuration in real space. The grey particles show positions directly computed from the N-body simulation, while the red particles show those positions predicted from mapping the action-space distribution in the bottom-right panel of Fig. 10. The two distributions almost precisely overlap. In both plots, the black arrowed curves show the trajectory of the progenitor orbit, while the blue curves show the mapping of the dashed line from Fig. 10. The blue curve is everywhere a much closer match to the stream particles than is the progenitor orbit.

space, we need to make a correction to the cluster’s action, as described by equation (32), to account for the variation in action down the stream. Evaluating equation (46) and equation (49) for the orbit I4, and taking $dL \sim 25 \text{ kpc km s}^{-1}$ and $dJ_r \sim 10 \text{ kpc km s}^{-1}$ from the bottom-right panel of Fig. 10, we predict errors in the real-space of up to $\sim 0.2 \text{ kpc}$ on account of the finite L distribution, and up to $\sim 0.15 \text{ kpc}$ on account of the finite J_r distribution. These errors would be serious enough to be seen in Fig. 13, and thus the correction is required. We note, however, that even these substantial errors are insignificant compared to the several-kpc discrepancy between the stream and the orbit.

7 THE CONSEQUENCES OF FITTING ORBITS

We confirmed in Section 4.3 that streams formed in the isochrone potential are not well delineated by orbits, and we provided a real-

istic example where this is the case. Many practical techniques attempt to use tidal streams to constrain the parameters of the Galactic potential, by erroneously assuming that such streams *do* delineate orbits. In this section, we briefly examine the consequences for such techniques of making this faulty assumption.

Our experiment is based on the simulated tidal stream of Fig. 13. This particular example is for a stream at apocentre: this is relevant, because many actual observed streams are discovered close to apsis, for example the Orphan stream (Belokurov et al. 2007) and GD-1 (Grillmair & Dionatos 2006).

We first create two sets of pseudo-data: one corresponding to the progenitor orbit, marked as a black line in Fig. 13, and one corresponding to the predicted stream track, marked as a blue line. Each pseudo-data set contains approximately 40 phase-space coordinates, sampled evenly from the length of the corresponding track, as shown in Fig. 13.

We now wish to measure the quality with which an orbit for a given set of isochrone-potential parameters can be made to fit the data. For the purposes of this exercise, we have assumed the functional form of the potential to be known. Further, we have granted ourselves pseudo-data with full and accurate positional and velocity information. Granting ourselves an unrealistically complete pseudo-data set simplifies considerably the matter of finding an orbit that is close to the best fitting one. In practice, one typically proceeds with one or more phase-space coordinates unknown, or known with substantially less precision than the others. In this case, our purpose is solely to demonstrate the errors that can be made by naively assuming that an observed stream can be fit with an orbit. Granting ourselves an unrealistically complete set of pseudo-data does not diminish our conclusions in this regard.

For each set of potential parameters, we choose an orbit as follows. We first select a datum near the centroid of the stream, and declare that our chosen orbit must pass directly through this datum. Although it may be that some nearby orbit, one that does not pass directly through this point, would make a better-fitting orbit, any such orbit must pass very close to the selected datum, because it is close to the centroid. Thus, such an orbit cannot be much better-fitting than one that passes directly through the datum. Having chosen a datum, for a given set of potential parameters, an orbit is defined.

Having chosen our orbit, a goodness-of-fit statistic χ^2 is calculated as follows. For each datum in the stream, with phase-space coordinate \mathbf{w}_i , a location along the orbit \mathbf{w}'_i is chosen that minimizes the square difference

$$(\mathbf{w}_i - \mathbf{w}'_i)^2. \quad (54)$$

Having obtained the \mathbf{w}'_i , the goodness-of-fit χ^2 is defined by

$$\chi^2 = \sum_{i,j} \frac{(w_{i,j} - w'_{i,j})^2}{\sigma_j^2}, \quad (55)$$

where j are the phase-space coordinates, and σ_j is the rms of $(w_{i,j} + w'_{i,j})/2$ over i . This χ^2 statistic provides a dimensionless measure of the phase-space distance between the best-fitting orbit in a given potential, and the pseudo-data.

If the pseudo-data set were a sample of a perfect orbit in some potential, we expect the value of χ^2 to be exactly zero, when the correct potential parameters are used. As the potential parameters are varied away from their true values, we expect the value of χ^2 to rise, as the best-fitting orbit becomes a steadily worse representation of the data. Hence, we expect minima in χ^2 to be associated with the potential parameters that are optimum, from the perspective of fitting an orbit to the data. We seek such minima by plotting

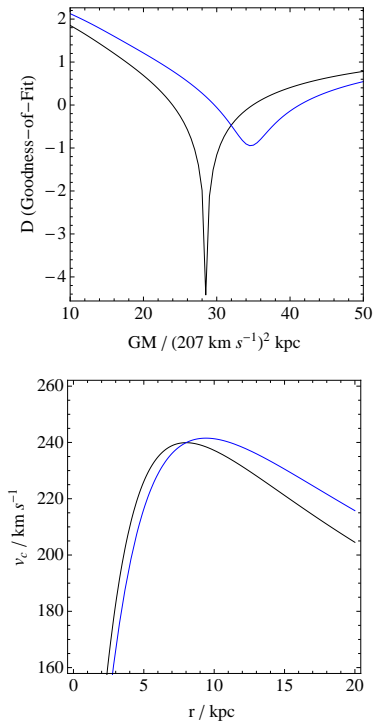


Figure 14. Top panel: goodness-of-fit χ^2 for each pseudo-data set, to the best-fitting orbit in the potential. The colours of the curves for each pseudo-data set identify it with the corresponding curve from Fig. 13 from which it was derived. Bottom panel: rotation curves for the optimum potential found for each pseudo-data set. In all cases, we have required that the circular velocity $v_c = 240 \text{ km s}^{-1}$ at $R_0 = 8 \text{ kpc}$. This reduces the potential to one of a single parameter; in this case, mass. The quality of the fit to the blue data set is significantly degraded, compared to that of the black. Utilising the high-curvature, blue data set as a proxy for an orbit causes us to overestimate the host mass by approximately 21 per cent.

the value of χ^2 over a range of likely values for the potential parameters.

7.1 Results

The upper panel of Fig. 14 shows the goodness-of-fit χ^2 , for the best-fitting orbit, in an isochrone potential with mass parameter GM as shown. For each value for GM , the isochrone parameter b is chosen such that the potential reproduces the fiducial rotational speed of $v_c = 240 \text{ km s}^{-1}$ at $R_0 = 8 \text{ kpc}$, since in practical usage one would generally require any acceptable potential to reproduce other observed features of the Milky Way galaxy, such as the circular velocity at the Solar radius. This has the effect of reducing the dimensionality of the search for the best-fitting solution to a single parameter.

Along each of the black and blue curves in Fig. 14, χ^2 has a minimum at the potential parameters for which the best-fitting orbit has been found. In the case of the black curve, which attempts to fit to pseudo-data derived directly from the progenitor orbit, the value of GM is correctly identified with high precision, thus validating the technique.

For the blue curve, which attempts to fit pseudo-data derived from the stream track, the quality of the fit at optimum GM is significantly degraded when compared to the black curve. This indicates that, although an optimal value for the mass parameter is be-

ing found, the fit to the orbit is still not perfect there. Furthermore, the value of GM for which the optimal fit is found is 21 per cent larger than the true value.

The attempt to constrain the potential parameters by using misaligned streams as proxies for orbits has led us to err. The high-curvature of the stream, relative to the orbits of the stars that comprise it, has incorrectly led the fitting procedure to a significantly larger enclosed mass, in order to provide the larger gravitational force necessary to produce a more highly-curved orbit. This can clearly be seen from the lower panel of Fig. 14, which shows the rotation curves for the optimum potentials for both sets of pseudo-data. In the case of the stream-derived pseudo-data, the circular speed of the optimum potential is significantly higher than the truth at those distances where our stream segment lies.

In conclusion, we find that there is a risk of substantial systematic errors in parameter estimation being made, if one attempts to constrain the potential using streams, and one assumes that streams perfectly delineate orbits. In practice, one would hope that the significant degradation of the minimum χ^2 of the fit to the stream-derived data, when compared to orbit-derived pseudo-data, would be noticeable. However, it is often the case that random noise in the measurements are sufficient to reduce the quality of fits such that such discrimination is not possible (Binney 2008; Eyre & Binney 2009b). If this is so, then even with the perfect error-free data used in this section, the uncertainty on the deduced mass parameter could not be better than ± 20 per cent. In practice, the uncertainty is likely to be much, much worse. Only by fitting stream data to physically-motivated stream tracks instead of orbits can we hope to overcome this limitation, and obtain the tantalising diagnostic precision proffered by the analysis of streams in such as Binney (2008).

8 NON-SPHERICAL SYSTEMS

We have investigated the formation of streams in spherical potentials, and demonstrated that they are not necessarily well modelled by orbits, but that with some prior knowledge of the system, we can accurately predict their tracks. However, many real stellar systems in the Universe are not spherical. In particular, our own Galaxy, whose potential we are interested in probing with streams, is significantly flattened.

In the case of spherical systems, the stream can only be misaligned with the progenitor orbit *within* the plane to which both stream and orbit are confined. Orbits in flattened potentials are generically three-dimensional as a result of the instantaneous orbital plane precessing around the potential's symmetry axis. Different parts of the stream have orbit planes which precess at different rates, so the stream is not strictly confined to a plane. Moreover, the plane that most nearly contains the stream generally differs from the instantaneous orbit plane of the progenitor. These complexities come on top of the misalignments within the best-fitting plane that we have studied in spherical potentials. They could well be the reason that all attempts to find a single orbit that fits the Sagittarius dwarf stream have had limited success (Fellhauer et al. 2006; Niederste-Ostholt et al. 2010). In this section, we investigate the formation of streams in a flattened Stäckel potential.

8.1 Stäckel potentials

Regular orbits in non-spherical potentials can be described by a system of three actions, but the actions and angles can be computed by

standard means only if the potential is a Stäckel potential (§3.5.3 of BT08). An exhaustive treatment of these potentials is given in de Zeeuw (1985) and de Zeeuw et al. (1986), from which we adopt our notation. The example we consider is an oblate axisymmetric potential, for which the appropriate coordinate system is that of prolate spheroidal coordinates, (λ, ϕ, ν) ; λ is constant on confocal ellipsoidal surfaces of revolution, while ν is constant on the hyperbolic surface of revolution that cut the ellipsoids orthogonally. Hence λ is a radial coordinate and ν is analogous to latitude. The coordinate system is specified by two negative quantities (α, γ) . The potential has the form

$$\Phi(\lambda, \nu) = -\frac{(\lambda + \gamma)G(\lambda) - (\nu + \gamma)G(\nu)}{\lambda - \nu}, \quad (56)$$

where de Zeeuw's function $G(\tau)$ is determined once the density profile $\rho(z)$ along the z -axis has been chosen (see e.g. equation (23), de Zeeuw et al. 1986). Thus, the model is completely specified by $\rho(z)$ and the scaling parameters (α, γ) . The actions for Stäckel potentials of this type are (J_λ, L_z, J_ν) , corresponding to motion in (λ, ϕ, ν) respectively.

8.2 Galaxy models with Stäckel potentials

de Zeeuw et al. (1986) shows that if one requires the density everywhere to be non-negative, it is not possible to formulate a Stäckel model in which the density $\rho(r)$ falls off with distance from the z -axis more rapidly than r^{-4} as $r \rightarrow \infty$. This is because an elementary density on the z -axis $\rho(z) = \delta(z - z_0)$ requires an off-axis density term that falls as r^{-4} . This behaviour rules out many classes of galaxy models, including discs with exponential density profiles. However, we can construct models in which the density falls more slowly than r^{-4} as $r \rightarrow \infty$. In particular, models with asymptotically flat rotation curves, i.e. those in which $\rho(r) \sim r^{-2}$, are allowed.

In the models used in this section, we specify the z -axis density profile

$$\rho_z(z) = \frac{-\gamma\rho_0}{(z^2 - \gamma)} = \frac{-\gamma\rho_0}{\tau}, \quad (57)$$

where we have made use of $z^2 = \tau + \gamma$. In this case, de Zeeuw's function $G(\tau)$ can be written in closed form (equation (49) with $s = 2$, de Zeeuw et al. 1986). Models specified by equation (57) become spherical at large radii and have a rotation curve that is asymptotically flat, with

$$\lim_{r \rightarrow \infty} v_c^2 = -4\pi G\rho_0\gamma. \quad (58)$$

In the core of these models, the surfaces of constant density are approximately ellipsoidal, with axis ratio¹

$$\frac{a_z^2}{a_R^2} = \frac{2q^2}{(1 - q^2)^2} (1 - q^2 + q^2 \log q^2), \quad (59)$$

where the central potential axis ratio $q = \sqrt{\gamma/\alpha}$. The models are completely specified by choosing a shape via q , a mass scale via ρ_0 , and a distance scale via γ . The combination of an asymptotic logarithmic 'halo' and a flattened 'disc' in these models allows them to make a fair representation of the observed properties of disc galaxies, although the lack of freedom in the models severely restricts the shape of the density distribution that can be achieved.

¹ Equation (46) in de Zeeuw et al. (1986) presents a formula for this quantity, but it is incorrect.

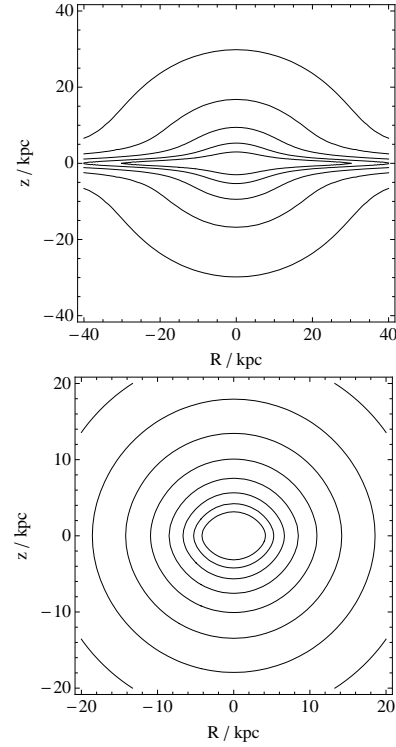


Figure 15. The upper panel shows contours of $\log \rho/\rho_0$ for the Stäckel model SP1, utilized in this section. The lower panel shows contours of the potential Φ for the same.

The potential used in this section, SP1, was chosen to simulate a galaxy with a massive disc. The axis ratio of the density distribution is fixed to be 10 near the solar radius, $R_0 = 8$ kpc, which is approximately the same ratio as for the (exponential) thin disc profile of the Milky Way (see Table 2.3 of BT08). The specification is completed by requiring the rotation curve to peak at $R_0 = 8$ kpc with a circular speed $v_c = 240$ km s⁻¹. The resulting parameters of the SP1 potential are: $\rho_0 = 3.61 \times 10^9 M_\odot \text{ kpc}^{-3}$, $\alpha = -29.64 \text{ kpc}^2$, $\gamma = -8.89 \times 10^{-3} \text{ kpc}^2$.

We note that the asymptotic circular velocity in this model is $v_c = 42$ km s⁻¹, which can be regarded as the halo contribution to the circular speed. The model is too centrally concentrated, and the halo contribution is too weak, to realistically model the Milky Way. However, it is highly flattened, and so makes an interesting example in which to study stream geometry. Contours of constant density and potential for this model are shown in Fig. 15.

8.3 Stream misalignment in the Stäckel potential SP1

We now consider the geometry of streams formed in the Stäckel potential SP1. Although the actions \mathbf{J} can be defined in terms of an integral over a single coordinate, closed-form expressions for \mathbf{J} do not exist. Instead, the integrals in the expressions for \mathbf{J} have to be evaluated numerically. Similarly, expressions for both the frequencies Ω and their derivatives $\nabla_{\mathbf{J}}\Omega$ can be derived, but not in closed form, and the integrals that they contain must also be evaluated numerically.

The expressions for \mathbf{J} and Ω appear in de Zeeuw (1985). The detailed expressions for $\nabla_{\mathbf{J}}\Omega$ are algebraically rather involved, and are presented in the appendix of Eyre (2010b). Here, we simply note that having evaluated these quantities for a particular orbit \mathbf{J}_0 ,

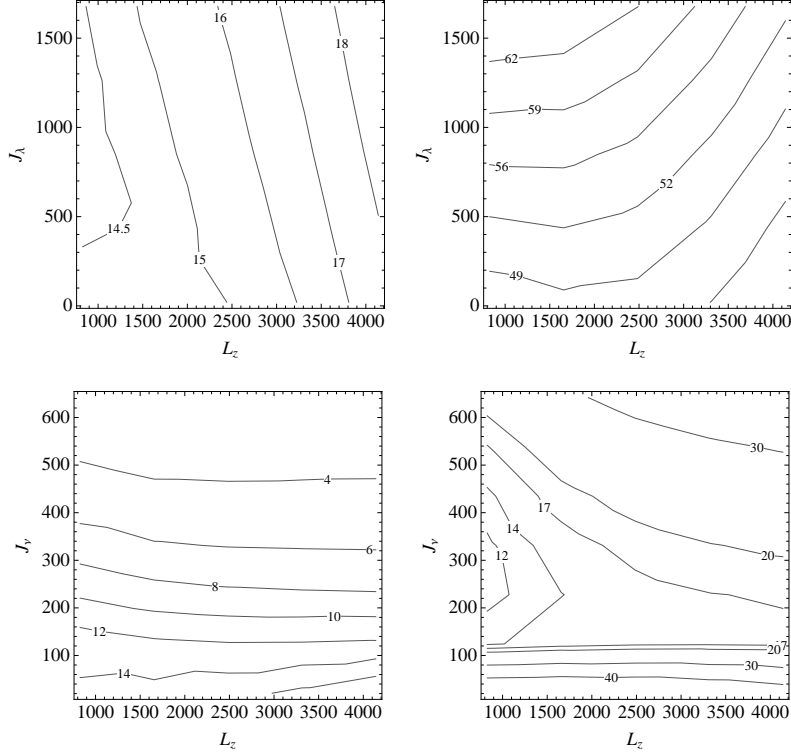


Figure 16. Details of the stream geometry for the Stäckel potential SP1. Left panels: contours for the misalignment angle ϑ , in degrees, between the principal eigenvector of \mathbf{D} and $\boldsymbol{\Omega}_0$, shown as a function of \mathbf{J} . Right panels: contours for the eigenvalue ratio λ_1/λ_2 . The top panels show the plane in action-space with $J_\nu = 20.7 \text{ kpc km s}^{-1}$, while the bottom panels show the plane in action-space with $L_z = 414 \text{ kpc km s}^{-1}$. The range of actions covers a variety of interesting orbits: details of orbits at the extremes of the range are given in Table 4

Table 4. The coordinate extrema of selected orbits from Fig. 16, illustrating the variety of orbits covered by that figure. The actions are expressed in kpc km s^{-1} , while the apses are in kpc.

J_λ	L_z	J_ν	R_P	R_a	$ z _{\text{max}}$
20	828	20	3.5	5	0.74
20	4140	20	20	26	2.5
1680	4140	20	14	70	7
1680	828	20	1.75	27	3
414	828	20	2	10	1.25
414	4140	20	16	38	3.5
414	4140	640	22	56	34
414	828	640	3	20	17

the eigenvectors $\hat{\mathbf{e}}_n$ and the eigenvalues λ_n are computed directly from the matrix $\mathbf{D}(\mathbf{J}_0) = \nabla_{\mathbf{J}}\Omega|_{\mathbf{J}_0}$ by standard methods.

The left panels of Fig. 16 show contour plots of the misalignment ϑ in angle-space between the principal direction of \mathbf{D} and the frequency vector $\boldsymbol{\Omega}_0$, where ϑ is calculated from equation (27), as was the case for systems of two actions. The right panels of the same figure show contours of the ratio λ_1/λ_2 . The range of actions shown in these plots covers a variety of interesting orbits; the apses of the orbits at the extremes of the range are described in Table 4.

As with the equivalent plots for the isochrone potential (Fig. 3), we see that the principal direction of \mathbf{D} is never perfectly aligned with $\boldsymbol{\Omega}_0$. In this very flattened potential, streams with low J_ν have the greatest degree of misalignment, at about ~ 15 deg. These orbits never go far from the disc. The misalignment dimin-

ishes with increasing J_ν , falling to ~ 4 deg for orbits with apses in z of some tens of kpc. Hence, in this very flattened potential, there is much more prospect for dramatic angle-space misalignment than the small misalignments we encountered with the isochrone potential (Fig. 3). Fig. 16 also shows that the eigenvalue ratio $\lambda_1/\lambda_2 > 10$ everywhere for the SP1 potential; thus, we conclude that highly elongated streams will form on all orbits which permit a cluster to be disrupted.

As with the spherical case, the precise behaviour of any given stream depends on both the potential and the action-space distribution of its stars. To proceed further we must again consider a specific example, by means of N-body simulation.

8.4 A stream in the Stäckel potential SP1

Fig. 17 shows the real-space trajectory of the orbit SO1, evaluated in the Stäckel potential SP1. This orbit has actions $(J_\lambda, L_z, J_\nu) = (252.3, 2618., 20.4) \text{ kpc km s}^{-1}$ and apses of approximately $R = (8, 18) \text{ kpc}$ in the galactic plane, and $z = (-2, 2)$ above and below the plane. It is thus fairly representative of an eccentric orbit that might be occupied by a globular cluster orbiting close to a galactic disc.

The cluster model C5 (Table 3) is a King model specified for the orbit SO1 according to the schema of Section 6.1. The model has the same mass and profile parameter as C1, and is very similar in all other attributes, because the orbit SO1 is similar to the orbit I4 for which C1 was specified. A 10^4 particle realization of the C5 was made by random sampling of the King model distribution function. This cluster was placed close to apocentre on the orbit

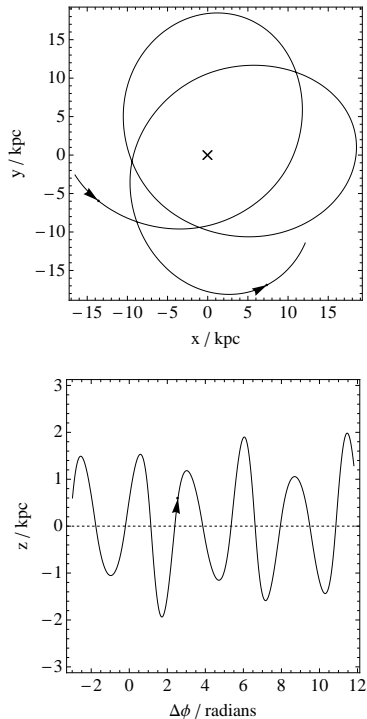


Figure 17. The real-space trajectory of the SO1 orbit in the Stäckel potential SP1. The upper panel shows a plan view of the galactic plane, while the lower panel plots height above the plane, z , against azimuthal coordinate, ϕ .

SO1 and evolved forward in time by the FVFPS tree code, with time step $dt = t_{\text{dyn}}/100$ and softening parameter ϵ as specified in Table 3. The total period of the simulation was 2.15 Gyr, or 7 complete radial oscillations.

8.4.1 Action-space distribution

Fig. 18 shows the evolution in time of the action-space distribution of this simulated cluster. Each column of panels shows the distribution at a different point in time. The upper panel in each row shows the orthographic projection of the actions onto the (L_z, J_λ) plane, while the lower panel of each row shows a similar projection onto the (L_z, J_ν) plane. In all panels, the appropriate projection of the mapped frequency vector, $\mathbf{D}^{-1}\Omega_0$, is shown as an arrowed black line.

The left hand column shows the actions when the cluster is near to its first pericentre passage. In the upper panel, the distribution is somewhat flattened, and oriented with positive gradient in $\Delta J_\lambda/\Delta L_z$. This behaviour is analogous with that seen in the top-right panel of Fig. 10: the motion of the cluster is predominantly in (λ, ϕ) , thus (J_λ, L_z) are good proxies for the radial action J_r and angular momentum L respectively. J_λ and L_z are therefore highly correlated for a cluster near apsis on this orbit, in analogy with the mechanism described by equation (53) in Section 6.2.

Meanwhile, the distribution in the lower panel is both narrow and oriented almost exactly along \hat{L}_z . We can understand the shape as follows. For this orbit, which is confined to be close to the plane, $J_\nu \sim J_z/2$, where the factor of 2 appears because J_ν is defined on a path restricted to only one side of the plane. J_z can be estimated by close analogy with equation (29). Hence, the spread in J_ν for a

cluster of velocity dispersion σ is approximately

$$\Delta J_\nu \simeq \frac{1}{2}\Delta J_z \sim \frac{1}{2\pi}\delta p_z \Delta z \simeq \frac{1}{2\pi}\sigma \Delta z. \quad (60)$$

By analogy with equation (31) we find

$$\frac{\Delta J_\nu}{\Delta L_z} \sim \frac{\Delta z}{2\pi R_p}, \quad (61)$$

where R_p is the galactocentric pericentre radius in cylindrical coordinates. Evaluating this expression for the orbit SO1 gives $\Delta J_\nu/\Delta L_z \sim 0.04$, which we see from the lower-left panel of Fig. 18 is close to exact.

The flat orientation of the lower-left panel we explain by pointing out that, as Fig. 17 shows, the motion in ν in this example is almost decoupled from the radial motion. This means that the ν coordinate need not be at apsis when the cluster is at pericentre, and thus the arguments of Section 6.2, which force a correlation between $J_\lambda \sim J_r$ and $L_z \sim L$ near pericentre, do not apply. For an orbit in which J_ν is more strongly coupled to the radial motion, we would expect to see the characteristic tilting of the (L_z, J_ν) distribution near pericentre and apocentre, as a correlation between J_ν and L is forced.

The middle column of panels in Fig. 18 shows the action-space distribution at the subsequent apocentre passage. Bound and unbound particles are shown in black and red, respectively. The action-space structure of the unbound particles in the upper panel bears striking similarity to that shown in Fig. 10, as might be expected since (J_λ, L_z) make good proxies for (J_r, L) . The same physical principle for the disruption of the cluster applies here as in the spherical case; that is, the particles will escape the cluster through the Lagrange points L_1 and L_2 by first travelling radially, so the action-space distribution will be compressed in this direction. Thus, the range of ΔL_z and ΔJ_ν for the unbound stars is about the same as in the left hand panels, but the range of ΔJ_λ is markedly less.

The right hand panels of Fig. 18 show the action-space distribution at the 7th apocentre passage. The structure is essentially the same as that of the middle panels, except that all particles are now unbound. Also plotted in each of the right hand panels is a dashed line, which has been least-squares fitted to the unbound particles. We note that the image of the frequency vector and the dashed line are highly misaligned in the upper-right plot; because of this, we expect the stream to be significantly misaligned with Ω_0 in angle-space.

In conclusion, we find that in very flattened potentials, disrupted clusters form an action-space distribution that is wholly analogous with, although necessarily more complicated than, that found for disrupted clusters in spherical potentials.

8.4.2 The effects of disc shocks

Unlike with a spherical potential, an axisymmetric potential allows for tidal forces other than those felt during pericentre passage to act upon an orbiting cluster. In particular, the passage of a cluster through a massive galactic disc will subject a cluster to a tidal force that is of comparable magnitude to that felt when close to pericentre.

The tidal stress imposed on a cluster at pericentre has a tensile component, which acts to strip stars from the cluster. Conversely, the tidal stress imposed by a disc passage is entirely compressive in nature. Hence, stars are not actively stripped from a cluster during a disc passage. Instead, the action of such ‘disc shocks’ is to heat the

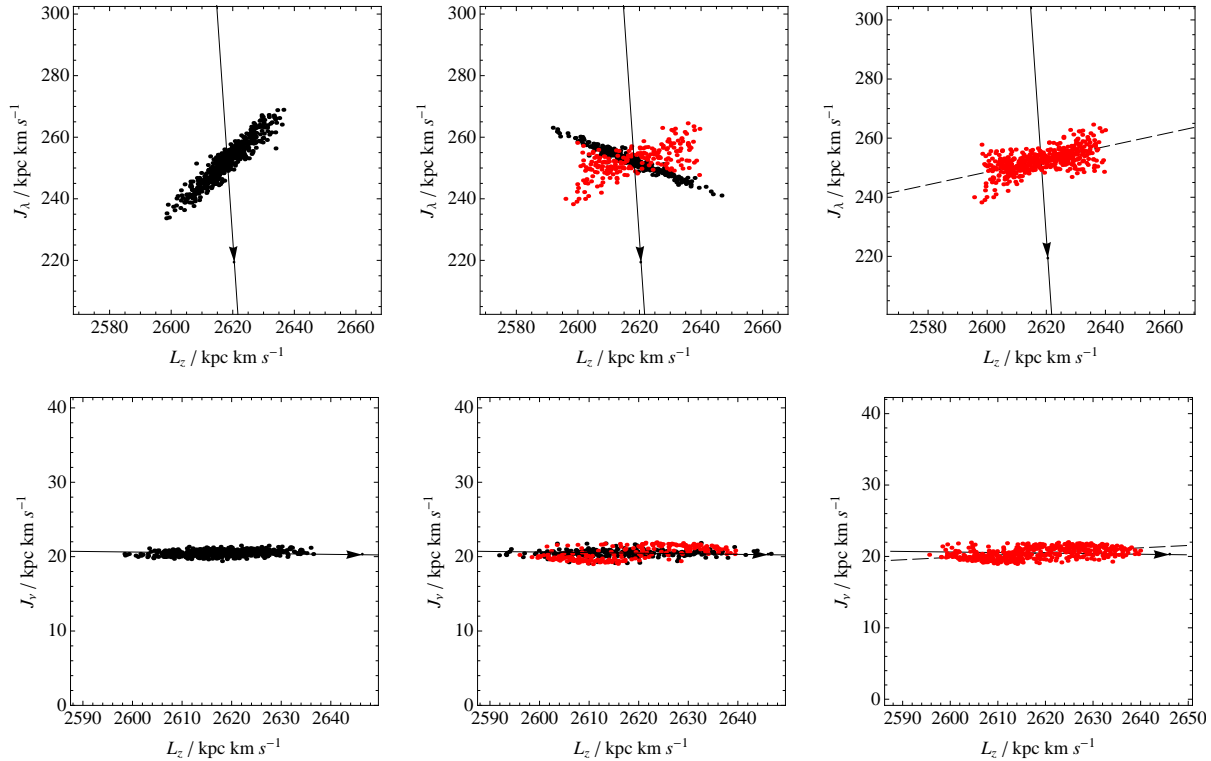


Figure 18. Action-space distribution for the simulated cluster C5, on the orbit SO1 in the Stäckel potential SP1, at various points in time. The upper panels show the orthographic projection of distribution onto the (L_z, J_λ) plane, while the lower panels show a similar projection onto the (L_z, J_y) plane. Distributions are shown at the following times: left panels, the first pericentre passage; middle panels, the subsequent apocentre passage; right panels, the 7th apocentre passage. Black particles are bound to the cluster, while red particles orbit free in the host potential. The dashed lines in the bottom panels are lines that have been least-squares fitted to the particles.

cluster, perhaps repopulating the outer edges of the cluster, which were depopulated during a previous pericentre encounter (Spitzer 1987, §5.2a).

The net effect of disc shocks on the stripping process is a faster and more complete disruption of the cluster than would take place for an unshocked cluster exposed to equivalent pericentric tidal stress. Since the vast majority of stars continue to be stripped at pericentre even when the effect of disc shocks is significant, the gross action-space distribution resulting from the stripping of a shocked cluster will remain as previously described. However, since the disc shocks act to increase the velocity dispersion of the cluster between stripping events, it is likely that the wings of the resulting action-space distribution will be populated with more stars than would otherwise have been the case.

8.4.3 Predicting the stream track

Fig. 19 shows the angle-space configuration for the simulated cluster near its 7th apocentre passage. The grey particles are for angles that have been computed directly from the output of the N-body simulation. The arrowed black line is Ω_0 , while the blue line is the map of the dashed-line from Fig. 18. In both projections, the blue line is a much superior match to the data than is the orbit.

Fig. 20 shows equivalent plots to those of Fig. 19, but in real space. The misalignment between the stream and the progenitor orbit in angle-space is seen to map into a large misalignment in real space. Attempting to constrain halo parameters by fitting orbits to the stream shown in Fig. 20 would not produce sensible results.

Conversely, the map of the dashed-line model for the action-space distribution, shown in Fig. 18, clearly provides an excellent proxy for the track of the stream. We note that, as per our expectation, there is significant distortion both in and out of the effective orbital ‘plane’.

9 CONCLUSIONS

We have studied the mechanics of the disruption of low-mass clusters, and the subsequent formation of tidal streams. In particular, we have examined the conditions required for the formation of tidal streams from such clusters, and to what extent such streams delineate the orbits of their stars. With regard to the latter, we are motivated by techniques that promise to constrain the form and parameters of the Galactic potential when observations of thin streams are analyzed under the assumption that such streams precisely delineate orbits (Binney 2008; Eyre & Binney 2009a; Willett et al. 2009; Newberg et al. 2010; Koposov et al. 2010).

We utilize action-angle variables extensively in our approach to the problem. These coordinates allow a convenient and natural description of the physical processes that occur in cluster disruption and stream formation. The stream has a structure in action-space that is formed at the point of disruption, and subsequently frozen for all time. The angle-space structure of the stream is the image of that action-space distribution under a linear map, which is itself a function of the host potential and the progenitor orbit only. This angle-space image elongates linearly with time, corresponding to

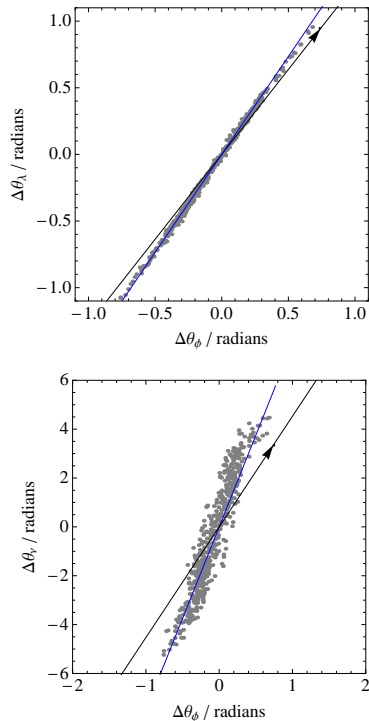


Figure 19. Angles for the N-body cluster shown in the right hand panels of Fig. 18. The blue line shows the predicted stream, resulting from the mapping of the dashed line from the same plots. The blue line is clearly a much better representation of the stream than is Ω_0 , represented by an arrowed black line.

the extension of the stream, but its shape remains otherwise unchanged. Disrupted clusters elongate to form streams because this linear map preferentially stretches the angle-space structure along a particular direction. We find this preferential stretch to occur for likely orbits in all the realistic potentials that we consider: the only exception is the spherical harmonic oscillator potential, in which clusters cannot be stripped at all.

The real-space structure of a stream is a function of the corresponding action-angle structure and the host potential. We have investigated the conditions required for a stream to be perfectly delineated in real space by its progenitor’s orbit. One necessary condition is that the angle-space stream be perfectly delineated by the frequency vector.

We have shown that this will always be the case for a stream formed in a Kepler potential. Conversely, we have shown that this is generally not the case for a stream formed in an isochrone potential: angle-space streams will generally be misaligned with the frequency vector by a few degrees. Since the isochrone potential is a more realistic representation of a galactic potential than is the Kepler potential, we infer that streams formed in galactic potentials will not generally be perfectly delineated by orbits. Indeed, it would appear that the alignment of streams with orbits is a property that is peculiar to the Kepler potential. Since streams exist in the outer parts of galaxies where the potential has a substantial monopole component, we propose this as an explanation for the observation that streams appear to be *approximately* delineated by the orbits of their stars.

We have examined the real-space manifestation of angle-space streams that are misaligned with their frequency vector. We find that the real-space effect depends on the orbital phase at which the

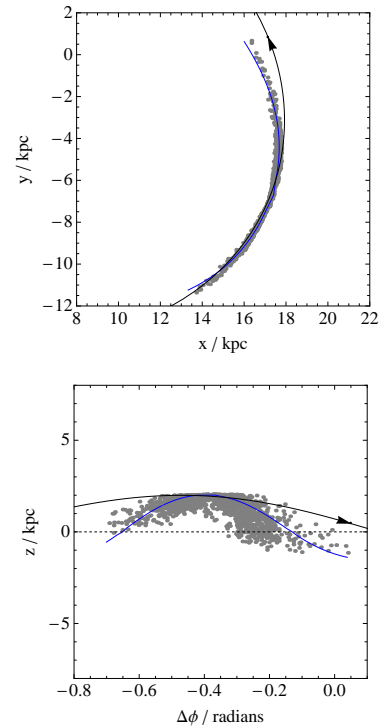


Figure 20. Real-space representation of an N-body simulation of cluster model C5 evolved on the orbit SO1, in the SP1 potential. The points are shown near the 7th apocentre passage following release. The black line shows the trajectory of an individual orbit; the blue line shows the predicted stream path.

stream is observed: at apsis, the stream track will have a curvature that differs from that of the progenitor orbit, while away from apsis the stream and its orbits will be spatially misaligned.

We have also examined the real-space effects of a finite action-space distribution for a stream. We conclude that, with a cluster described by a large, but realistic, velocity dispersion, knowledge of the angle-space structure and the progenitor orbit is no longer sufficient to accurately predict the real-space track of a stream. We describe a first-order correction to the actions of the stream stars that is deduced from observables, plus an estimate of the time elapsed since the initial cluster disruption event. This correction suffices to allow accurate predictions of real-space tracks to be made for streams formed from larger clusters.

We have confirmed the validity of our analyses with the use of N-body simulations of the disruption of clusters in the isochrone potential. These show that disrupted clusters indeed form streams that are poorly represented by the trajectory of the progenitor orbit.

We have used these simulations to inform an explanation of the action-space structure of disrupting clusters. We find that the action-space distribution of a disrupted cluster takes a characteristic shape, the details of which depend on the cluster model, the cluster orbit and the host potential. We are able to explain all features of this distribution in terms of the basic physical processes that apply to clusters undergoing tidal disruption. We further show that by utilising a simple, straight-line model of the action-space distribution, we are able to predict the real-space stream track of a stream with very high accuracy.

We have briefly examined the consequences of our findings for techniques that attempt to constrain the Galactic potential under the

assumption that streams can be fit with orbits. We utilize such an algorithm to attempt to constrain the mass of an isochrone potential, subject to the rotation speed at the Solar circle being equal to a fiducial value, and subject to input pseudo-data being fit with an orbit. We validate our optimisation procedure using input pseudo-data for a track that perfectly delineates an orbit. When the input pseudo-data are for a simulated stream in which the track shows an increased curvature with respect to orbits in the correct potential, the algorithm fails to identify the correct parameters: in our example, the response of the algorithm was to report an optimum mass parameter 21 per cent greater than the true value, albeit with a substantially decreased quality-of-fit compared to attempts to fit to pseudo-data representative of a true orbit. We conclude that large systematic errors can be made when attempting to optimize potential parameters under the assumption that streams act as proxies for orbits.

We have examined stream formation in a flattened, axisymmetric Stäckel model, which provides a fair approximation to the potential near a massive galactic disc. We find that in this potential the principal direction of the linear map is misaligned with the frequency vector by ~ 10 deg. Hence in highly flattened potentials like this, streams will not be well represented by orbits.

We performed an N-body simulation of a disrupting cluster on an approximately planar orbit in the flattened potential. We found that the angle-space misalignment between the stream and the frequency vector is indeed large, and that the resulting real-space track is very poorly represented by the progenitor orbit. However, we again find that a simple straight-line model of the action-space distribution predicts the corresponding real-space stream track with superb accuracy. We also find that in our Stäckel example, the action-space distribution resulting from the disruption of clusters is directly comparable to that found in the isochrone potential, confirming the generality of our earlier conclusions.

The consequences of our findings for potential-optimization techniques are significant: large systematic errors are possible if orbits are fitted to streams. Before attempting such activity, it is now necessary to check whether the segment of the stream in question could be legitimately represented by an orbit. Similarly, is also important for this check to be performed retrospectively for those streams—e.g. Orphan stream analysis of Newberg et al. (2010) and the GD-1 analysis of Koposov et al. (2010)—that have already been used to constrain the parameters of the Galactic potential, since the validity of those analyses is now in question.

Such a check could always be performed using N-body simulation, where it is believed that the progenitor model, the orbit and the applicable potential are well known. However, the application of the techniques in this paper would constitute a more general approach, in which the implications of an incorrect model or orbit can be readily addressed.

The techniques presented in this paper depend on the ability to compute action-angle variables from conventional phase-space coordinates, and vice versa. In this paper, we have restricted our consideration to models for which global transformation relations can be written down. The only such models are those with potentials of the Stäckel type, which includes all spherical potentials as a limiting case (de Zeeuw 1985). However, it is difficult to construct a realistic flattened galaxy model that is satisfactory in all respects whilst restricted to using only Stäckel potentials. In general, one would like to work with more sophisticated models for which no general transformation between action-angle variables and phase-space coordinates can be made.

Fortunately, the “torus machine” (McMillan & Binney 2008)

enables the actions, the frequencies and their derivatives to be accurately and quickly computed for regular orbits in realistic Galactic potentials. By utilising the torus machine, the techniques explored in this paper could be extended to work with such models. This approach could be used to investigate the impact on streams of orbital resonances and chaos: with the torus machine one can construct approximate angle-action variables even for potentials that support chaos (Kaasalainen & Binney 1994). Resonances and chaos play rather a small role in the dynamics of axisymmetric galactic potentials, but one might expect the sensitivity of chaotic orbits to their initial conditions to lead to a measurably more rapid spread of tidal streams in chaotic rather than integrable regions of phase space.

If a check—however performed—confirms that the stream is well modelled by an orbit, then diagnosing the potential by the fitting of orbits to streams is appropriate. However, if the stream is not well modelled by an orbit, as will generally be the case, the technique of fitting orbits should not be used.

In such circumstances, one might resort to N-body shooting methods to compute stream tracks to feed to an optimization algorithm (Johnston et al. 2005). However, the computational expense of such a technique would be a major burden, and would severely limit the quality of the optimization.

The results of this paper present a possible alternative. We have found that with simple models of the action-space distribution of a disrupted cluster, such as can be readily obtained from a single N-body simulation, we can reliably and accurately predict the track of a stream, even when it diverges significantly from the trajectory of the progenitor orbit. In principle, we can compute these tracks with no more computational effort than it takes to integrate an orbit. Existing techniques for constraining potential parameters by fitting orbits could be readily adapted to fit stream tracks instead.

To achieve this goal, the key hurdle is the development of a predictive theory for the action-space structure of a disrupted cluster, valid for any problem parameters of our choice. A possible approach would be to use N-body simulations to obtain the action-space distribution for a small number of cluster models on a set of possible orbits, for a range of potentials. The resulting distributions could be used as a basis set, which would be interpolated and distorted to provide an estimate for the action-space structure for any given cluster on any chosen orbit. The required distortions for changes to cluster model and orbit parameters have already been touched upon in this paper, although in order to be of practical use, a complete quantitative theory of these distortions will be required.

In the future, the techniques presented here may well be applicable to the Sagittarius dwarf stream. In this paper we have assumed that our low-mass clusters do not affect the host potential. This may not be true in the case of a heavy Sagittarius progenitor. Further study of the effect of a live host potential on the mechanics of stream formation will be required for the techniques to be reliably applicable to the Sagittarius dwarf stream. Also, the action-space structures discussed will be, in part, composed of dark matter in the case of streams formed from dwarf spheroidal galaxies. Further investigation of the stripping of satellites using models including both dark particles and stars will be required to determine which parts of the stream will remain visible, and which will be composed solely of dark matter.

ACKNOWLEDGMENTS

We would like to thank Ben Burnett and the other members Oxford dynamics group for helpful discussions. AE would like to acknowl-

edge the support of both PPARC/STFC and the Rudolf Peierls Centre for Theoretical Physics at Oxford during the preparation of this work. Parts of this paper were derived from work previously presented in the thesis of Eyre (2010b).

REFERENCES

- Belokurov V., et al., 2006, *ApJ*, 642, L137
 Belokurov V., et al., 2007, *ApJ*, 658, 337
 Binney J., 2008, *MNRAS*, 386, L47
 Binney J., Merrifield M., 1998, *Galactic Astronomy*. Princeton University Press, Princeton
 Binney J., Tremaine S., 2008, *Galactic Dynamics: Second Edition*. Princeton University Press, Princeton
 Choi J., Weinberg M. D., Katz N., 2007, *MNRAS*, 381, 987
 de Zeeuw T., 1985, *MNRAS*, 216, 273
 de Zeeuw T., Peletier R., Franx M., 1986, *MNRAS*, 221, 1001
 Dehnen W., Odenkirchen M., Grebel E. K., Rix H., 2004, *AJ*, 127, 2753
 Eyre A., 2010a, *MNRAS*, 403, 1999
 Eyre A., 2010b, DPhil thesis, University of Oxford
 Eyre A., Binney J., 2009a, *MNRAS*, 399, L160
 Eyre A., Binney J., 2009b, *MNRAS*, 400, 548
 Fellhauer M., Belokurov V., Evans N. W., Wilkinson M. I., Zucker D. B., Gilmore G., Irwin M. J., Bramich D. M., Vidrih S., Wyse R. F. G., Beers T. C., Brinkmann J., 2006, *ApJ*, 651, 167
 Grillmair C. J., 2006, *ApJ*, 645, L37
 Grillmair C. J., 2009, *ApJ*, 693, 1118
 Grillmair C. J., Dionatos O., 2006, *ApJ*, 643, L17
 Grillmair C. J., Johnson R., 2006, *ApJ*, 639, L17
 Helmi A., White S. D. M., 1999, *MNRAS*, 307, 495
 Jin S., Lynden-Bell D., 2007, *MNRAS*, 378, L64
 Johnston K. V., Hernquist L., Bolte M., 1996, *ApJ*, 465, 278
 Johnston K. V., Law D. R., Majewski S. R., 2005, *ApJ*, 619, 800
 Kaasalainen M., Binney J., 1994, *Physical Review Letters*, 73, 2377
 King I. R., 1966, *AJ*, 71, 64
 Koposov S. E., Rix H., Hogg D. W., 2010, *ApJ*, 712, 260
 Londrillo P., Nipoti C., Ciotti L., 2003, *Memorie della Societa Astronomica Italiana Supplement*, 1, 18
 Majewski S. R., Skrutskie M. F., Weinberg M. D., Ostheimer J. C., 2003, *ApJ*, 599, 1082
 McGlynn T. A., 1990, *ApJ*, 348, 515
 McMillan P. J., Binney J. J., 2008, *MNRAS*, 390, 429
 Montuori M., Capuzzo-Dolcetta R., Di Matteo P., Lepinette A., Miocchi P., 2007, *ApJ*, 659, 1212
 Newberg H. J., Willett B. A., Yanny B., Xu Y., 2010, *ApJ*, 711, 32
 Newberg H. J., Yanny B., Willett B. A., 2009, *ApJ*, 700, L61
 Niederste-Ostholt M., Belokurov V., Evans N. W., Peñarrubia J., 2010, *ApJ*, 712, 516
 Odenkirchen M., Grebel E. K., Dehnen W., Rix H., Yanny B., Newberg H. J., Rockosi C. M., Martínez-Delgado D., Brinkmann J., Pier J. R., 2003, *AJ*, 126, 2385
 Odenkirchen M., Grebel E. K., Kayser A., Rix H., Dehnen W., 2009, *AJ*, 137, 3378
 Spitzer L., 1987, *Dynamical Evolution of Globular Clusters*. Princeton University Press, Princeton
 Tremaine S., 1999, *MNRAS*, 307, 877
 Willett B. A., Newberg H. J., Zhang H., Yanny B., Beers T. C., 2009, *ApJ*, 697, 207
 Yanny B., Newberg H. J., Grebel E. K., Kent S., Odenkirchen M., Rockosi C. M., Schlegel D., Subbarao M., Brinkmann J., Fukugita M., Ivezić Ž., Lamb D. Q., Schneider D. P., York D. G., 2003, *ApJ*, 588, 824
 York D. G., et al., 2000, *AJ*, 120, 1579

This paper has been typeset from a $\text{\TeX}/\text{\LaTeX}$ file prepared by the author.